Review Article

Nano Research
2023, 16(4): 4468–4487

ISSN 1998-0124 CN 11-5974/O4
https://doi.org/10.1007/s12274-023-5457-9

Microenvironment regulation of M-N-C single-atom catalysts towards oxygen reduction reaction

Li Zhang[1,2], Qinglei Meng[1], Ruixue Zheng[1,3], Liuqing Wang[1,3], Wei Xing[1,3] (✉), Weiwei Cai[2] (✉), and Meiling Xiao[1,3] (✉)

[1] *State Key Laboratory of Electroanalytical Chemistry, Changchun Institute of Applied Chemistry, Chinese Academy of Sciences, Changchun 130022, China*
[2] *Sustainable Energy Laboratory, Faculty of Materials Science and Chemistry, China University of Geosciences, Wuhan 430074, China*
[3] *School of Applied Chemistry and Engineering, University of Science and Technology of China, Hefei 230026, China*

Received: 23 November 2022 / **Revised:** 23 December 2022 / **Accepted:** 24 December 2022

ABSTRACT

The development of cost-effective, robust, and durable electrocatalysts to replace the expensive Pt-based catalysts towards oxygen reduction reaction (ORR) is the trending frontier research topic in renewable energy and electrocatalysis. Particular attention has been paid to metal-nitrogen-carbon (M-N-C) single atom catalysts (SACs) due to their maximized atom utilization efficiency, biomimetic active site, and distinct electronic structure. More importantly, their catalytic properties can be further tailored by rationally regulating the microenvironment of active sites (i.e., M–N coordination number, heteroatom doping and substitution. Herein, we present a comprehensive summary of the recent advancement in the microenvironment regulation of M-N-C SACs towards improved ORR performance. The coordination environment manipulation regarding central metal and coordinated atoms is first discussed, focusing on the structure–function relationship. Apart from the near-range coordination, long-range substrate modulation including heteroatom doping, defect engineering is discussed as well. Besides, the synergy mechanism of nanoparticles and single atom sites to tune the electron cloud density at the active sites is summarized. Finally, we provide the challenges and outlook of the development of M-N-C SACs.

KEYWORDS

single-atom catalyst, oxygen reduction reaction, microenvironment regulation, active site structure, electronic structure

1 Introduction

In the modern society, fossil energy crisis and environment pollution have driven the research and development of sustainable and environmentally friendly energy technology [1–3]. For example, electrochemical energy conversion and storage technology including fuel cells and Zn-air batteries (ZABs) holds a great promise for clean power generation because it can convert chemical energy directly into electrical energy with high energy conversion efficiency and zero carbon emission [4–6]. However, their performance is seriously affected by the sluggish oxygen reduction reaction (ORR) at cathode due to the multi-electron proton transfer process of ORR [7]. Although Pt-based materials have been demonstrated effective to accelerate ORR kinetics, their scarcity and high cost severely hinder the commercial application [8–12]. Consequently, searching for efficient, inexpensive, and durable ORR electrocatalysts has become the most attractive research topic in this field [13–17].

Initiated by the pioneering work on cobalt phthalocyanine as a promising non-precious metal ORR catalyst [18], increasing enthusiasm has been directed towards metal–nitrogen ($M–N_x$) coordinate structured molecular catalysts. A breakthrough was achieved when Yeager et al. found the catalytic activity and stability can be boosted after a pyrolysis process [19]. Since then, pyrolyzed metal-nitrogen-carbon (M-N-C) catalysts have been dominant in the non-precious metal catalyst community. Thanks to the rapid development of high-resolution characterization techniques and diverse synthetic strategies, pyrolyzed M-N-C catalysts encounter unprecedented new opportunities. The active site structure is identified as single metal atom coordinated with nitrogen atoms, thus catalysts with maximum metal atom utilization are categorized as M-N-C single atom catalysts (SACs) [20–22]. Due to their unique structure, strong charge transfer occurs between central metal and surrounding atoms [23, 24]. Therefore, M-N-C SACs usually possess distinct electronic structure and thus perform excellent ORR activity and selectivity [25, 26].

The past decades have witnessed significant progress in developing M-N-C SACs for ORR. Combining the theoretical calculations and experimental results, the structure–function relationship between $M–N_x$ coordination and the catalytic properties is well understood, which in turn, serves as a guideline for the rational regulation of M-N-C SACs towards enhanced performance [27–31]. Generally, according to the Sabatier principle [32], the moderate adsorption energy is significant for boosting the performance of the catalysts. The weaker adsorption energy would inhibit the interaction between the reactant/intermediate and the catalysts, whereas the stronger

Address correspondence to Meiling Xiao, mlxiao@ciac.ac.cn; Weiwei Cai, caiww@cug.edu.cn; Wei Xing, xingwei@ciac.ac.cn

adsorption energy means that the active sites would be blocked and hindered for the next catalytic cycle. As the adsorption process is initiated by the overlapping of oxygen p orbital with d orbital of metal sites for most of the M-N-C catalysts, the position of the d-band has been recognized as the descriptor for the adsorption strength. On this basis, proper tune on the d-band center is essential to improve the ORR performance of M-N-C catalysts. M-N-C SACs with different central metal atoms (i.e., Fe [33], Co [34], Mn [35], Mg [36], Ce [37], etc.) have been developed, and their activity has been discovered to correlate with the d/p orbital electronic states of metal center. Among these catalysts, Fe based catalyst showed optimum d-band center, which means the moderate binding strength and the best ORR activity in the volcano type plot. On this basis, if we could modify the electronic states of Fe centers towards weaker binding strength with oxygen intermediates, its ORR activity could reach the apex of volcano plot. Utilizing the synergy between two adjacent metal atoms [38], a dual-atom site was designed [39], and it displayed superior activity to its single-atom counterpart. Since the electronic states of central metal are co-determined by the metal element, coordinated atoms, and substrate, proper tune on the coordinated atoms has been proven effective in tailoring ORR activity [40]. Recent research revealed that the spin manipulation can be a universal strategy to regulate the electronic structure of M-N-C SACs via introducing polar XO_2 (X represents S, Se, and Te) groups [41]. A linear relationship between spin moments of Fe centers and Fe 3d-band center was found in this work, which resulted in regulation of adsorption energy and intrinsic ORR activity. Regulating the coordination number and replacing N with other heteroatoms (i.e., sulfur (S) [42]) can enhance the ORR activity of M-N-C SACs. Although S is not directly coordinated with central metal atom, it can exert an electronic modulation effect through M-N-C-S long-range charge transfer [43]. Beyond that, defecting engineering and synergetic nanoparticle/single atom site construction can modify the electronic structure of M-N-C, thus, optimizing the intermediate binding energy on the active site towards boosted ORR kinetics [44–47].

In this review, we present a comprehensive summary of the microenvironment regulation of M-N-C SACs towards ORR, emphasizing the insights into the active site structure–catalytic property relationship. We first introduce the regulation of central metal and coordinated atoms regarding element diversity and coordination number, highlighting the crucial role of the electronic states of central metal site in determining ORR performance. Furthermore, we summarize the detailed discussion on incorporating axial ligands and/or the heteroatoms adjacent to the M–N_x site, defect engineering, and synergistic site construction that would modify the electronic structure of active site through long-range interaction. Finally, we provide the challenges and prospects of the development of M-N-C catalysts. We expect that this review will elucidate the design guidelines for achieving high-performance ORR catalysts, and inspire efforts to expedite further advancement in this field.

2 Regulation of central metal

2.1 Single-metal atom

For M-N-C SACs, the overlap between the d/p/s orbital of central metal and the p electrons of ORR intermediates determines the binding strength of ORR intermediates and the resulting ORR performance. Consequently, regulating the electronic structure of central metals via altering metal elements seems to be an effective approach to ideal catalytic activity [48]. Both theoretical calculations and experimental results demonstrate the ORR performance of M-N-C SACs follows a volcano type plot, with the trend as Fe-N_4 > Co-N_4 > Cu-N_4 > Mn-N_4 [49]. Due to the moderate binding energy of ORR intermediates, Fe-N_4 site locates nearest to the apex of the volcano type plot and promisingly shows the highest activity [50, 51]. On this basis, Fe-N-C SACs have attracted the most attention [25, 52–61]. For instance, Chen et al. prepared Fe-N-C SAC with abundant edge-Fe-N_4 sites using a self-sacrificing template method [62]. The half-wave potential ($E_{1/2}$) of Fe-N-C SAC reached 0.89 V in alkaline medium, which was better than that of commercial Pt/C. Xing's group reported a metal-organic-framework-confined pyrolysis strategy to prepare Fe-N-C SACs [63]. The optimal sample pyrolyzed under 950 °C, denoted as Fe-N-C-950 catalyst, exhibited excellent ORR activity ($E_{1/2}$ = 0.78 V) in 0.1 M $HClO_4$ solution (Fig. 1(a)). The ^{57}Fe Mossbauer spectra revealed that the high ORR activity could be attributed to the high spin Fe-N_4 configuration [64–66]. Despite the superior ORR activity, Fe-based catalysts suffer from poor stability caused by oxygen-containing radical attack, which is generated by the Fenton reaction between Fe^{2+} and H_2O_2 [67–69]. To improve the stability of Fe-based catalysts, two approaches are generally considered. The first one is adjusting the coordination environment surrounding the central Fe atom [70–75]. For instance, Wu et al. revealed that regulating the local carbon structure and promoting high active and unstable S1 (pyrrolic N-coordinated low spin Fe-N_4-C_{12}) sites transformed into high stable and less active S2 (pyridinic N-coordinated middle/high spin Fe-N_4-C_{10}) sites could enhance the stability [25]. This transition process can be monitored via ^{57}Fe Mössbeauer spectra. Besides, detailed regulation mechanism would be introduced in later chapters. The other one is seeking for highly efficient non-Fe based catalyst with low Fenton reactivity.

Co-based catalysts with lower Fenton reactivity have been extensively investigated as the most promising alternative to Fe-N-C SACs [34, 76]. For example, Wu et al. synthesized Co-N-C catalyst with abundant Co-N_4 sites and the $E_{1/2}$ reached 0.83 V in 0.5 M H_2SO_4 (Fig. 1(b)) [77]. Owing to the mitigated Fenton effect, Co-N-C catalyst displayed admirable stability by showing only 35 mV negative shift in $E_{1/2}$ after 30,000 accelerated stress tests (AST) in the range of 0.6 to 1 V, which proved the huge potential of Co-N-C catalyst to replace Fe-based catalyst. In a recent study by Shao and co-workers [34], Co-N-C demonstrated four-time enhanced durability compared with a similarly synthesized Fe-N-C counterpart. The suppressed chemical oxidation of catalysts and active site demetallation of Co-N-C SAC was responsible for its superior durability [34, 78]. However, the fuel cell performance using Co-N-C SACs as cathodic electrocatalysts is inferior to that of Fe-N-C SACs. Therefore, in order to achieve the practical application of Co-based catalyst, one strategy is to improve the activity of Co-N_4 catalyst by increasing the density of active sites. The other one is to boost the intrinsic activity of Co site by enhancing the adsorption energy of ORR intermediates on Co-N_4 site as it is located at the weak binding side of volcano plots [79, 80].

Apart from Co-N-C SACs, Mn-N-C SACs have been exploited to replace Fe-based catalysts because of their low-cost and optimal stability [81–83]. For instance, Xu et al. certified that Mn-N-C catalyst was more stable in fuel cell durability test than Fe-N-C catalysts at a constant potential of 0.65 V in H_2-air conditions (Fig. 1(c)) [84]. To get insights into the improved stability of Mn-N-C catalyst, density functional theory (DFT) calculations were conducted to simulate the metal stripping process of Mn-N_4 and Fe-N_4. The lower leaching free energy of Mn-N_4 compared to that of Fe-N_4 strongly verified the higher stability of the former. Although Mn-based catalysts exhibit such excellent stability, their ORR activity is unsatisfactory in comparison with Fe-based

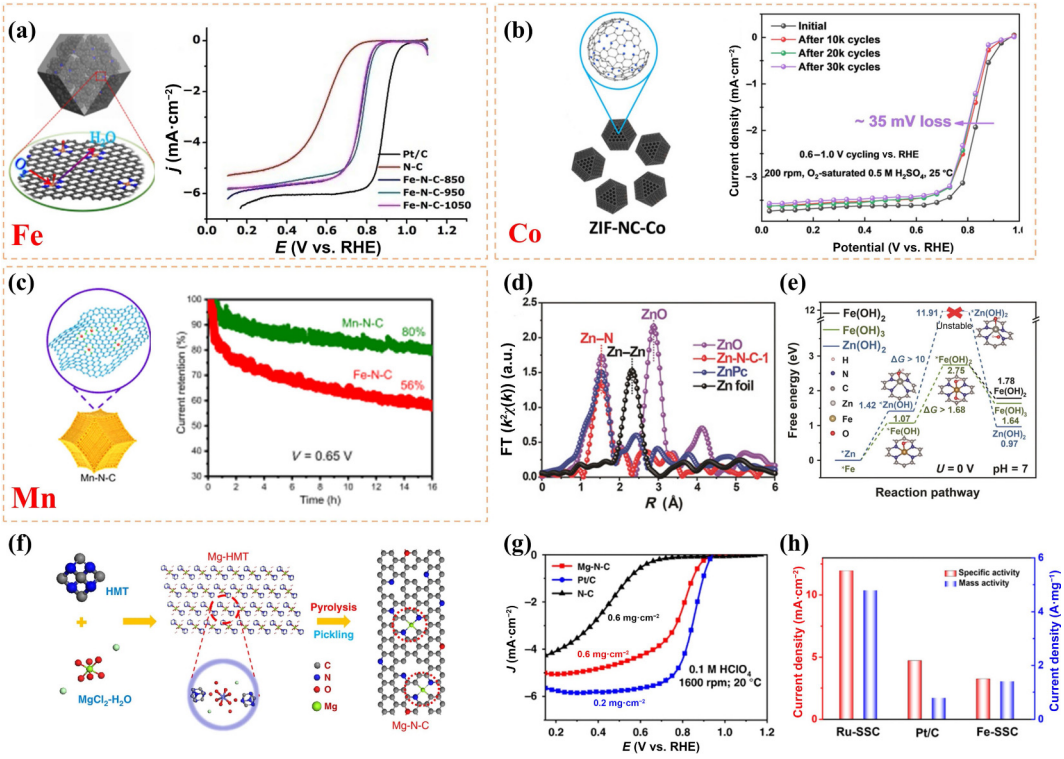

Figure 1 (a) The structure (left) and ORR activity of Fe-N-C catalysts (right) [63]. (b) The schematic (left) and stability test of Co-N-C catalyst (right) [77]. (c) The schematic of Mn-N-C catalyst on the left and membrane electrode assembly (MEA) durability tests for Mn-N-C and Fe-N-C catalysts on the right [84]. (d) Fourier transforms of extended X-ray absorption fine structure (FT-EXAFS) spectra of the Zn-N-C-1 catalyst and standard samples. (e) Free-energy diagrams for metal corrosion process of $Zn(OH)_2$, $Fe(OH)_2$, and $Fe(OH)_3$ [87]. (f) Synthesis process of Mg-N-C and (g) the electrochemical performance in 0.1 M $HClO_4$ [36]. (h) The Specific activity and Mass activity of Ru-SSC and standard samples [95]. (a) Reproduced with permission from Ref. [63], © American Chemical Society 2018. (b) Reproduced with permission from Ref. [77], © Wiley-VCH GmbH 2021. (c) Reproduced with permission from Ref. [84], © American Chemical Society 2020. (d) and (e) Reproduced with permission from Ref. [87], © Wiley-VCH Verlag GmbH & Co. KGaA, Weinheim 2019. (f) and (g) Reproduced with permission from Ref. [36], © Liu, S. et al. 2020. (h) Reproduced with permission from Ref. [95], © American Chemical Society 2019.

catalysts. This discrepancy could be attributed to low intrinsic activity and low density of Mn-N_4 sites [85]. Consequently, future research efforts should be directed towards improving the intrinsic activity and/or increasing the site density of Mn-N_4 sites [35, 86].

In sharp contrast to Fe, Co, Mn, the d-orbital of Zn atoms is completely filled, which prevents the formation of high-valent Zn ions that will degrade the electrode and electrolyte membranes [87]. Inspired by this, Wei et al. developed an atomically dispersed Zn-based catalyst (denoted as Zn-N-C-1) to catalyze ORR [87]. The active site structure was confirmed as Zn coordinated with four N atoms by Fourier transforms of the extended X-ray absorption fine structure spectra (FT-EXAFS) (Fig. 1(d)). The as-prepared Zn-N-C-1 catalyst with an ultrahigh-loading of Zn (9.33 wt.%) displayed high activity in both acidic and alkaline electrolytes, with $E_{1/2}$ of 0.746 and 0.873 V in 0.1 M $HClO_4$ and 0.1 M KOH electrolytes, respectively, surpassing Fe-N-C catalyst, which confirmed the significant importance of high-loading for M-N-C SACs. In addition, it possessed outstanding stability. DFT calculations were performed to investigate the excellent stability of the Zn-N_4 site by computing the formation free energy of *OH adsorbed on metal sites. It was found that the formation energy of *Zn(OH) (1.42 eV) is higher than that of *Fe(OH) (1.07 eV) (Fig. 1(e)). When two *OH attached to the same metal site, the metal atom tended to dissociate. The formation free energy of *$Zn(OH)_2$ (10.49 eV) was higher than *$Fe(OH)_2$ (1.68 eV). These results imply that Zn-N_4 site is more resistant to corrosion than Fe-N_4 site in ORR process. More interestingly, the research of the active center atom has extended to other transition metal elements. For instance, Xing et al. designed an effective Cr-N_4 site for the first time [88]. The $E_{1/2}$ of Cr-N-C catalyst in 0.1 M $HClO_4$ approached to that of the Fe-N-C counterpart. Besides, the suppressed Fenton reaction activity of Cr-N_4 site contributed to higher stability than that of Fe-N-C. A recent study revealed that rationally constructing Cu-N_4 sites onto edge-enriched carbon could activate the pristine inert Cu sites in catalyzing ORR [89]. The as-designed Cu-N_{2+2}-C catalyst exhibited superior ORR activity ($E_{1/2}$ = 0.88 V) to commercial Pt/C ($E_{1/2}$ = 0.85 V) in alkaline electrolytes. Furthermore, Cu-N_{2+2}-C catalyst possessed excellent discharge performance and long-term charge/discharge stability, which suggested that Cu could be a promising candidate of the non-Fe ORR catalysts.

In addition to the transition metals mentioned above, the main group metals (Mg [36], Ca [90], Sn [91], Sb [92, 93], and Se [94]) can also serve as active sites for ORR. Generally, the main-group metals in s-block have fewer valence electrons, thus usually exhibit single valence state. On this basis, s-block elements are expected as ideal active centers that would be effective to alleviate Fenton reactions. For example, Chen et al. synthesized Ca-N, O/C catalyst with atomically dispersed Ca atoms [90]. The optimized p-orbital electron structure of Ca facilitated the adsorption of ORR intermediates and electron transfer. As a result, Ca-N, O/C catalyst displayed exceptional ORR activity and durability. Besides, through directly pyrolyzing Mg-based metal-organic-framework (denoted as Mg-HMT) and subsequently acid leaching, Mg-N-C catalyst with optimized electronic configuration was prepared (Fig. 1(f)) [36]. In contrary to the principle in d-band metals, an up-shift of p-band center was proposed to cause decreased binding strength with the intermediates on Mg-N-C catalyst, thus leading to the high ORR activity ($E_{1/2}$ = 0.79 V) in 0.1 M $HClO_4$ (Fig. 1(g)). The main group metals in p-block could also be activated by coordinating with N atoms. Jiao et al. proved that the p orbital of positively charged Sb in Sb-N_4 sites can easily interact with the 2p

orbital of O_2 [96]. Besides, Sn-N-C catalyst with moderate oxygen adsorption/desorption properties was employed as cathode catalyst in fuel cells [91], which showed superior fuel cell performance under hydrogen-air condition. Beyond the metal elements, non-metallic element in p-block, Se is able to constitute ORR active sites [94]. For instance, atomically dispersed Se atoms on nitrogen doped carbon substrates were prepared by high-temperature annealing. The resultant catalyst, denoted as Se@NC-1000, exhibited remarkable long-term durability and satisfactory discharge power density in ZABs. This work provides the possibilities of extending the research of SACs from metal to nonmetal centers.

Apart from transition metals and main group metals, earth elements are also found to exhibit ORR activity and draw widespread attention in recent years. For example, Ce coordinated with four N atoms and six O atoms were reported active for ORR [37]. To be specific, the prepared Ce-N-C catalyst performed excellent activity with E_{onset} and $E_{1/2}$ of 1.04 and 0.862 V, respectively, which was superior to most of the reported M-N-C catalysts. The excellent performance of Ce-N-C catalyst was further confirmed in fuel cell test, delivering high power density of 0.525 W·cm^{-2} under 2.0 bar H_2/O_2 condition. Notably, the Ce-N-C is more advantageous in eliminating Fenton effect by its powerful ability to catalyze H_2O_2 decomposition.

To further improve ORR activity of M-N-C SACs, noble metal centers are designed. For instance, Ir-N-C SAC with atomic dispersed Ir-N_4 site was constructed in the research of Chen's group [24]. Due to the unique electronic structure of Ir-N_4 sites, the catalyst displayed a record-high turnover frequency of 24.3 e$^-$·site^{-1}·s^{-1} at 0.85 V vs. RHE. Beyond that, Xing et al. successfully fabricated Ru-N-C SAC with Ru-N_4 active sites (denoted as Ru-SSC) [95]. Ru-SSC showed higher specific activity and mass activity than commercial Pt/C catalyst and Fe-SSC catalyst in acidic solution (Fig. 1(h)). More interestingly, Ru-SSC presented superior stability to Pt/C by showing only 17 mV loss in $E_{1/2}$ after 20,000 cycles in potential cycling stability tests. DFT calculations suggested that excellent activity and stability originated from appropriate *OH adsorption energy and low Fenton activity.

2.2 Bi-atom active site

Although single atoms sites have shown considerable ORR activity and stability, there remains a certain room for the performance improvement to rival commercial Pt/C. For instance, Co-N-C SACs can mitigate Fenton effect, but suffer from lower intrinsic activity due to the weak binding strength with ORR intermediates. Recent studies revealed that constructing bi-atom active site could effectively tailor the electronic states of the single-metal atom site, thus achieving desirable catalytic properties [97, 98]. For instance, Xing et al. for the first time reported homonuclear bi-atom Co-based catalysts containing Co_2-N_5 sites via controlling the Zn/Co ratio in the precursor [99]. The presence of bi-atom site was confirmed by direct observation of two conjoint Co atoms with a distance of 2.1–2.2 Å in aberration-corrected HAADF-STEM images (Figs. 2(a) and 2(b)). Combining FT-EXAFS spectroscopy and theoretical calculations, the active site structure was confirmed as Co_2-N_5. On the Co_2-N_5 site, spontaneous *OH adsorption from water dissociation would modify the electronic structure of the pristine Co site, thus facilitating the rate-determining step (RDS) ($*O_2 + H^+ + e^- \rightarrow *OOH$) towards boosted ORR activity. As expected, the ORR performance of Co_2-N_5 sites was 12 times higher than Co-N_4 and approached to commercial Pt/C catalyst in 0.1 M $HClO_4$ solution. The *OH regulation mechanism was also proposed by Sun and co-workers [38]. In their study, ZnCo-N_6 site exhibited superior ORR performance to both Zn-N_4 and Co-N_4 sites. The theoretical calculations pointed out the geometric advantage of di-atom site, on which the O–O bond elongated from 1.23 to 1.43 Å (Fig. 2(c)). The extension of the O–O bond length suggested that ZnCo-N_6 is more conducive to the cleavage of O_2 at the first step of ORR process. In a recent study by Chen et al., IrCo-N-C catalyst with heteronuclear bi-atom IrCo-N_5 site was fabricated by pyrolyzing the Ir-doped ZnCo-ZIF in high temperature under flowing Ar/H_2 atmosphere (Fig. 2(d)) [100]. The incorporation of Ir was proposed to alter the d-orbital energy level of Co and thus inducing the re-arrangement of d-electron toward stronger affinity with ORR intermediates (Fig. 2(d)). A higher energy gap between antibonding states and bonding states observed on IrCo-N_5 corresponded to stronger Co–O bond. In line with the theoretical prediction, IrCo-N-C catalyst owned excellent performance with high $E_{1/2}$ of 0.911 V, superior to the Co-N-C ($E_{1/2}$ = 0.85 V) and Ir-N-C ($E_{1/2}$ = 0.845 V) counterparts (Fig. 2(e)). Moreover, when assembled into a ZAB, IrCo-N-C catalyst delivered a high open-circuit voltage of 1.46 V and a peak power density of 138.8 mW·cm^{-2}, outperforming the commercial Pt/C+Ir/C (1.43 V, 110.5 mW·cm^{-2}). In contrary to Co-N-C SACs, Fe-N-C SACs are criticized for the extremely strong adsorption energy of oxygen, which results in considerable energy barrier for the *OH desorption ($*OH + H^+ + e^- \rightarrow H_2O$). To weaken the binding energy of ORR intermediates on Fe site, Xing et al. designed a bi-atom FeCo-N_5 site to stabilize the electron-withdrawing OH ligand, which can act proactively as an energy level modifier to empower easy intermediate desorption [101]. As expected, the superb activity of FeCo-N_5 site can be validated by showing the highest kinetic current density (J_k) of 7.245 mA·cm^{-2} at 0.85 V, which was 20 and 64 times higher than that of single-atom Fe-N_4 and Co-N_4 site, respectively (Fig. 2(f)). Furthermore, the geometric merits endowed the catalyst with decreased H_2O_2 yield (2%) (Fig. 2(g)). Inspired by this study, Wen's group investigated ORR activity of three FeCo-N_6 isomers adsorbed with ORR intermediates (i.e., *O, *OH, and $*O_2$) [102]. It was found that FeCo-N_6-I (each metal atom coordinated with four nitrogen atoms) with *OH or $*O_2$ ligands promisingly displayed the highest ORR activity. A similar configuration was reported by Sun et al., who verified that FeNi-N_6-I contributed to the majority of ORR activity [103]. Constructing bi-atom sites can not only induce electronic and/or geometric structure regulation, but also modulate spin-state to optimize the adsorption/desorption behaviors on metal sites. For example, Zhang et al. discovered that the construction of bi-atom FeMn-N_6 site could regulate Fe-spin state [104].The electron energy loss spectrum (EELS) confirmed the co-existence of Fe and Mn elements. And their distance was estimated to be 0.25 ± 0.02 nm (Fig. 2(h)), which proved the successful fabrication of FeMn-N_6 site. The adjacent Mn-N_x induced spin-state transition of Fe to accelerate ORR kinetics. As a result, FeMn-N_6 site exhibited excellent ORR activity with $E_{1/2}$ of 0.928 V in 0.1 M KOH solution, surpassing the Fe-N_4 sites. The extraordinary ORR performance was further certified in ZAB test, where Fe, Mn-N-C catalyst delivered a high power density of 160.8 mW·cm^{-2} and long-term durability. Beyond the heteronuclear di-atom site, Fe_2-N_6 site was reported by Xie and co-workers [105]. Similarly, the intermediate species of *OOH would adsorb on the adjacent Fe atoms via bridge-cis model, which is beneficial for its subsequent dissociation. In summary, both theoretical and experimental studies confirmed that the geometric configuration and element type of bi-atomic sites are crucial to the final catalytic performance [106], which provides insights into the design and synthesis of efficient ORR catalysts containing bi-atom sites.

2.3 Non-bonded dual-atom sites

Recently, non-bonded dual-atom sites are emerging as superior active site to the single-atom site because of the long-range

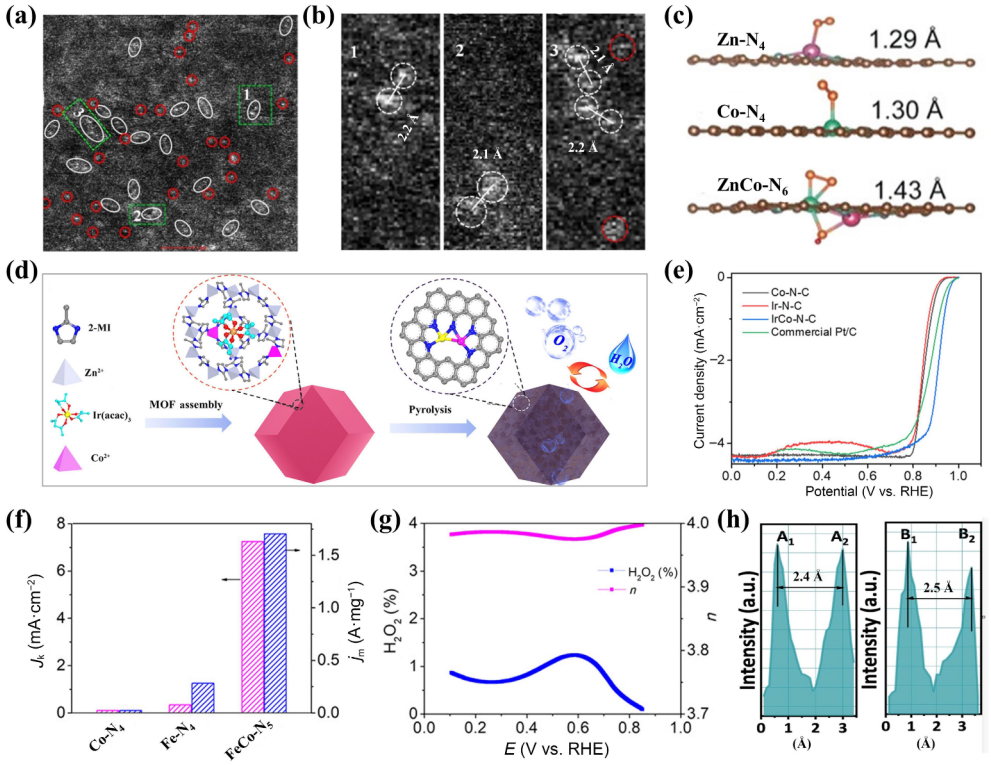

Figure 2 (a) and (b) Co_2-N_5 site in HAADF-STEM images [99]. (c) Optimized geometry of O_2 adsorption configuration on the Zn-N_4, Co-N_4, and ZnCo-N_6(OH) systems [38]. (d) The synthesis process of IrCo-N-C. (e) The ORR performance of IrCo-N-C catalyst [100]. (f) Kinetic current density comparison of Co-N_4, Fe-N_4, and FeCo-N_4 catalysts. (g) H_2O_2 yield and electron transfer number of FeCo-N_5/C site [101]. (h) Statistical Fe–Mn distance in the observed diatomic pairs of FeMn-N_6 site [104]. (a) and (b) Reproduced with permission from Ref. [99], © Elsevier Ltd. 2018. (c) Reproduced with permission from Ref. [38], © Wiley-VCH Verlag GmbH & Co. KGaA, Weinheim 2019. (d) and (e) Reproduced with permission from Ref. [100], © American Chemical Society 2021. (f) and (g) Reproduced with permission from Ref. [101], © American Chemical Society 2019. (h) Reproduced with permission from Ref. [104], © Yang, G. G. et al. 2021.

coupling effect between the two isolated sites [107, 108]. For instance, FeCo-N doped in porous carbon with homogenous Fe-N_4 and Co-N_4 sites (denoted as $FeCo_2$-NPC-900) was designed by pyrolyzing metalloporphyrin MOFs at 900 °C (Fig. 3(a)) [109]. The $FeCo_2$-NPC-900 catalyst exhibited high ORR activity with $E_{1/2}$ of 0.87 V in 0.1 M KOH, exceeding that of single-atom Fe-N-C and Co-N-C counterparts. Such an enhancement was proposed to originate from the synergetic effect between Fe-N_4 and Co-N_4 sites. In order to clarify the synergetic effect, DFT calculations were conducted by Bu and co-workers [110]. The synergetic effect between the dual-atom sites (Fe/Co-N_4) optimized adsorption energy of *O and thus decreased the reaction barrier of RDS towards faster ORR kinetics (Fig. 3(b)). Besides, the density of states (DOS) revealed that dual-atom sites possessed a minimum band gap of 0.29 eV (Fig. 3(c)), implying increased electronic conductivity and accelerated electron transfer. Ni-N_4 site is also employed to regulate the ORR performance of Fe-N_4 site, as Zhao et al. reported a Fe/Ni-N_4 doped in porous carbon, which displayed an 84 mV positive shift in $E_{1/2}$ compared with single-atom Fe-N-C catalyst [111]. However, in another work by Chen and co-workers [112], Fe-N_4 was proposed to modulate the coordination environment of Ni-N_4 site, triggering optimized adsorption energy of ORR intermediates on the Ni-N_4 site. In addition to optimizing adsorption energy, dual-atom sites are able to regulate the spin polarization and promote O–O dissociation as well. For instance, the incorporation of Mn-N_4 site induced the selective formation of low-spin Fe^{II}-N_4 (D1) [113]. The increased D1 (75.6%) content in Fe/Mn-N-C was responsible for its higher activity than Fe-N-C (50%) (Figs 3(d) and 3(e)). At the same time, there was an electronic effect in the Fe/Mn-N-C sample, as X-ray absorption near-edge structure (XANES) spectra revealed obvious electron transfer between Fe-N_4 and Mn-N_4 (Fig. 3(f)). Therefore, it is the combination of increased D1 content and electronic modulation effect that contributed to the enhanced ORR performance of Fe/Mn-N-C catalyst. While in the case of Cu/Zn-N-C catalyst [114], the presence of Zn-N_4 denoted electron to Cu-N_4 not only strengthens oxygen adsorption on Cu-N_4 site, but also stretches O–O bond towards easier breaking. Based on the above analysis, the synergy between dual-atom sites can effectively promote oxygen adsorption and the subsequent reduction reaction. However, precise synthesis of dual-atom sites and the in-depth mechanistic understanding are still challenging, which required more efforts towards innovation in synthetic strategies and the development of the more advanced characterization tools.

3 Regulation of coordinated atoms

As the active site is composed of central metal and coordinated atoms, regulation of coordinated atoms could exert an electronic modulation effect on the central metal, and thus tailoring the binding strength with ORR intermediates towards boosted intrinsic ORR activity [115]. In this section, we would like to introduce the coordinated atom regulation from the three aspects including nitrogen coordination (number and type), heteroatom substitution (i.e., S [70], P [116], O [86], etc.), and axial coordination ligand.

3.1 Nitrogen coordination

3.1.1 Coordination number

Due to the difference of electronegativity between the metal and the nitrogen atom, there would exist an electron transfer from M to N in M-N-C SACs. Therefore, the number of coordinated N atom will play a crucial role in determining the electron effect on M–N_x sites [79]. In a theoretical study conducted by Kasai and co-workers, M-N_2 sites with metal centers at weak binding side of volcano plot (i.e., Co and Ni) were found to promote the four-

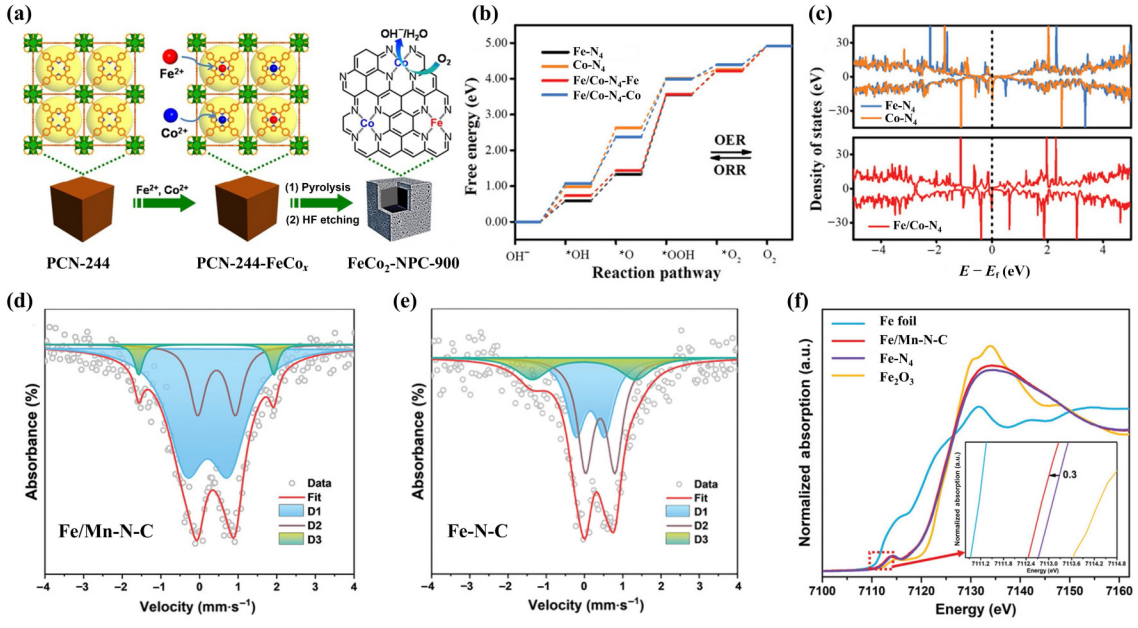

Figure 3 (a) Illustration of the stepwise fabrication of $FeCo_2$-NPC-900 [109]. (b) Free energy diagrams for ORR on the single-atom and bi-atom sites. (c) DOS patterns of Fe-N_4 and Co-N_4 (up) and Fe/Co-N_4 (down) [110]. (d) and (e) ^{57}Fe Mössbauer absorption spectra of Fe/Mn-N-C (d) and Fe/N-C (e). (f) Normalized Fe K-edge XANES of Fe/Mn-N-C (inset: enlarged near-edge absorption curves) [113]. (a) Reproduced with permission from Ref. [109], © Wiley-VCH Verlag GmbH & Co. KGaA, Weinheim 2017. (b) and (c) Reproduced with permission from Ref. [110], © Wiley-VCH GmbH 2022. (d)–(f) Reproduced with permission from Ref. [113], © Wiley-VCH GmbH 2022.

electron ORR pathway, and the RDS on these sites changed from oxygen adsorption to *OH desorption [117]. This result implies that a decreased coordination number is beneficial for the metal elements at weak binding side. The hypothesis was validated by a recent work from Zhang's group [118]. They synthesized the Ni-N-C catalyst with monodispersed Ni-N_2 active sites utilizing the space confinement effect of SiO_2 nanospheres. Ni-N_2 active sites endow the catalyst with higher ORR performance ($E_{1/2}$ is 0.88 V and J_k is 20.0 mA·cm^{-2}), surpassing the catalyst with Ni-N_4 sites [119]. Besides, the superiority of the Ni-N_2 sites enabled an outstanding power density of 120 mW·cm^{-2} in ZABs [118]. In addition to Ni, Mg-N_2 was reported active to catalyze ORR. For example, Chen et al. have successfully designed Mg-N-C catalysts with Mg-N_2 as active sites [36]. The as-prepared Mg-N-C catalysts showed excellent performance with $E_{1/2}$ up to 0.79 V in 0.1 M $HClO_4$. While for Co-N-C SACs, Co-N_3 sites were also proposed to improve ORR activity and selectivity. More interestingly, a theoretical study by Sun et al. revealed that the Co-N_3 site embedded in graphene was superior to Pt/C with lower energy barrier (0.38 eV vs. 0.80 eV for Pt/C) at the RDS (the decomposition of *OOH) of ORR [120]. Inspired by the DFT prediction, Zhao et al. designed Co-N_3 sites by *in-situ* pyrolytic Co/Zn-ZIF-67 and demonstrated that Co-N_3 site was favorable for O_2 adsorption [121]. Beyond that, Sardroodi et al. demonstrated that Cu-N_3 embedded graphene can serve as a highly efficient catalyst for ORR [122], which deserves further study in the future. From the above results, it can be found that the weaker binding strength is, the smaller coordination number should be, which will provide some insights for the rational regulation of coordination number.

In contrast to the metals at weak binding side, higher N coordination number is favorable for Fe-N-C SACs that located nearest to the apex. For example, Shui et al. designed Fe-N_x sites with different N-coordination numbers by controlling the annealing temperature [123]. To be specific, by pyrolyzing the precursor at 300, 500, and 1000 °C the catalysts with Fe-N_1, Fe-N_3, and Fe-N_4 sites, respectively, were obtained (Fig. 4(a)). The superiority of Fe-N_4 over other sites was confirmed by the highest ORR activity of the catalyst pyrolyzed at 1000 °C (FeNC-1000) (Fig. 4(a)). Besides, the coordination number affected the stability with a sequence as Fe-N_4 > Fe-N_3 > Fe-N_1. In addition to determining the intrinsic activity of the active site, the coordination number of N will affect the neighboring atom and determine active site density. For instance, Zhang et al. demonstrated a weaker neighboring effect of Fe-N_4 site than Fe-N_3 [124], which was beneficial for improving the density of Fe-N_4 sites. Higher coordination number more than 4 was theoretically proposed to reduce the energy barrier of *OH desorption process and promote the intrinsic activity of Fe-N-C SACs [125]. Wang et al. confirmed that the catalyst with Fe-N_5 sites (denoted as FeN_5–C/G) performed higher ORR activity than that of the catalysts with Fe-N_4 sites [126]. The ZABs of FeN_5–C/G catalysts showed a high specific capacity of 798 mA·h·g^{-1} and remarkable long-term stability, superior to the Pt/C-based battery. Besides, Yang et al. designed Fe-N_5 site by grafting a pyridine group to the Fe-N_4 site on the surface of graphene (left in Fig. 4(b)) [127]. The as-obtained catalyst, denoted as FePc/AP-GA displayed a 40 mV positive shift in $E_{1/2}$ compared with Fe-N_4 counterpart (right in Fig. 4(b)). In their study, geometric and electronic effect of this novel structure was believed to contribute to the higher activity, yet not being specifically clarified. While in the research work by Chen and co-workers, they conducted DFT calculations to unveil the origin of activity enhancement on Fe-N_5 sites [128]. They discovered that electron diminution of Fe d_{z2} orbital could accelerate the last electron transfer process, thus boosting the ORR kinetics. By pyrolyzing polymerized o, -phenylenediamine, ferric chloride, and carbon black, Su et al. prepared P*p*PD-Fe-C catalyst with Fe-N_6 as active sites that Fe coordinated with four N atoms in the plane and two pyridine-N in the axial direction (Fig. 4(c)) [129]. This unique structure enabled improved activity and stability in compared with the control samples, which provide a new inspiration for the design of superior performance of SACs.

3.1.2 *Coordinated N type*

As known to all, the types of N participating in M–N_x sites include pyrrole-N and pyridine-N, which will cause varying degrees electron redistribution and local electrical field for M-N_4 site [50]. Combining experimental results and theoretical calculations, Cao'

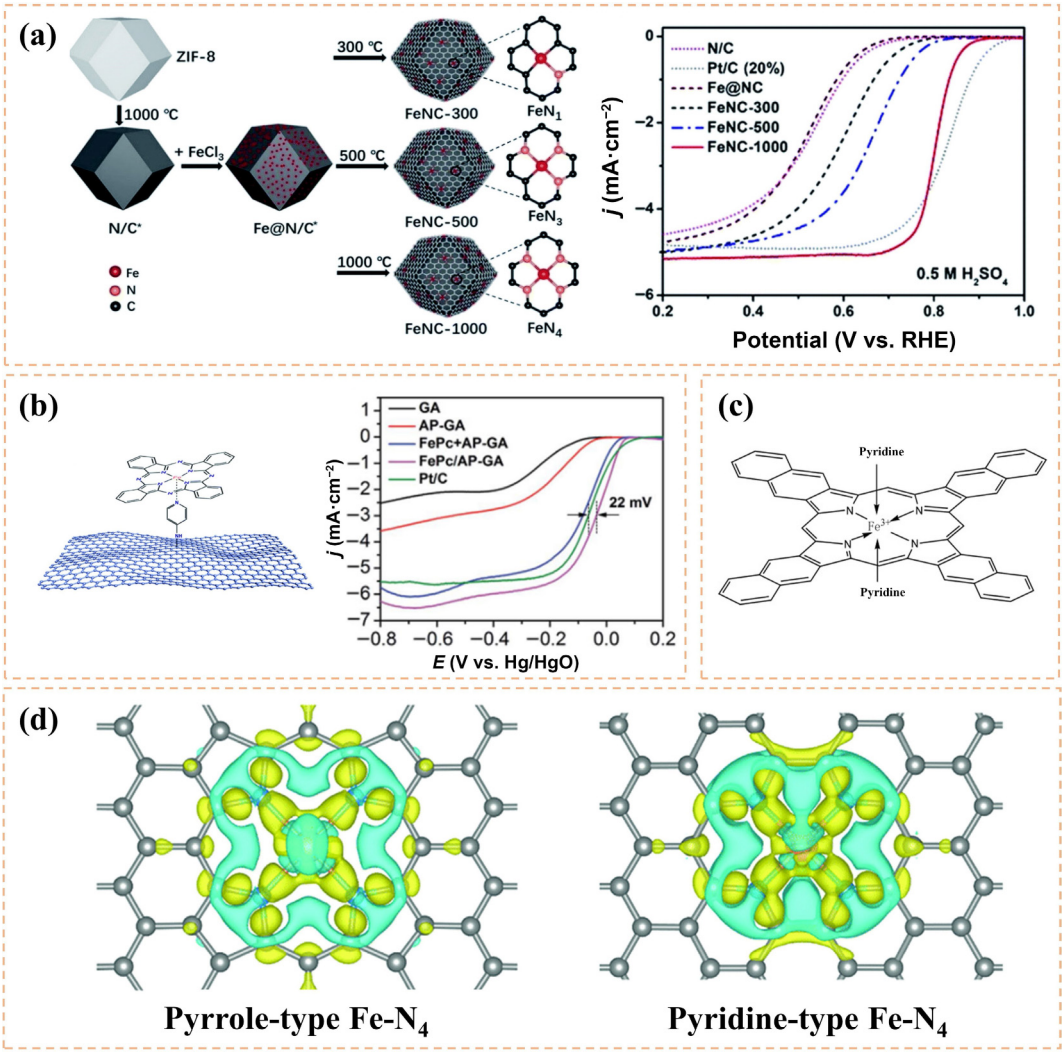

Figure 4 (a) The synthesis process for FeNC-300/500/1000 (left) and LSV curves of FeNC-300/500/1000 (right) [123]. (b) The structure of active sites and ORR activity of FePc/AP-GA catalyst [127]. (c) The structure of P*p*PD-Fe-C catalyst [129]. (d) Calculated charge density difference of pyrrole-type Fe-N_4 (left) and pyridine-type Fe-N_4 (right) [33]. (a) Reproduced with permission from Ref. [123], © The Royal Society of Chemistry 2019. (b) Reproduced with permission from Ref. [127], © The Royal Society of Chemistry 2018. (c) Reproduced with permission from Ref. [129], © WILEY-VCH Verlag GmbH & Co. KGaA, Weinheim 2014. (d) Reproduced with permission from Ref. [33], © The Royal Society of Chemistry 2020.

s group proved the superiority of pyrrole-type Fe-N_4 site [130]. Following this study, Xie and coworkers prepared a Fe-N-C catalyst with high-purity pyrrole-type Fe-N_4 sites by transforming pyridine-N to pyrrole-N via the assistance of NH_3 pyrolysis [33]. The as-designed catalyst (HP-Fe-N_4) exhibited extremely high ORR performance with the E_{onset} of 0.95 V and $E_{1/2}$ of 0.86 V, surpassing the pristine Fe-N_4 counterpart. Besides, it showed lower H_2O_2 yields (< 2%) than that of Fe-N_4 catalyst (3.5%), demonstrating pyrrole-type Fe-N_4 sites possess higher selectivity for four-electron ORR pathway. The DFT calculations revealed that more electron depletion in pyrrole-type Fe-N_4 than pyridine-type Fe-N_4 (Fig. 4(d)), which would accelerate the first electron transfer step of ORR. In line with their study, Jaouen and his co-work confirmed the higher ORR activity of pyrrole-type Fe-N_4 [65]. However, they found that the pyrrole-type Fe-N_4 would degrade to ferric oxide during ORR process using *in-situ* ^{57}Fe Mössbauer spectroscopy, while the pyridine-type Fe-N_4 with lower activity exhibited superb stability. To unveil the origin of higher stability of pyridine-type Fe-N_4, Yin et al. computed the free energy change of Fe atoms leaching process [40]. The free energy change of pyridine-type Fe-N_4 was 1.64 eV lower than that of pyrrole type Fe-N_4 (0.67 eV) with O_2 adsorbed, implying higher stability of the former. In addition, a shorter Fe–N bond length of pyridine-type Fe-N_4 contributed to its stability as well. In contradictory with the above opinions, Wang and co-workers pointed out pyridine-type Fe-N_4 was more active than pyrrole-type Fe-N_4 [131]. The former required only 0.20 eV energy for *OOH dissociation, while pyrrole-type Fe-N_4 necessitated much higher energy of 0.72 eV. Wu et al. also proved the excellent activity of pyridine-type Co-N_4 site as the catalyst delivered high ORR performance with E_{onset} and $E_{1/2}$ of 0.97 and 0.86 V, respectively [132]. Employing DFT calculations, Zhang and coworkers demonstrated superior ORR activity of pyridine-type Co-N_4 to the pyrrole-type one. However, both the 2-electrons pathway and 4-electrons pathway may proceed on pyridine-type Co-N_4 [133], while only 4-electrons pathway is favorable on pyrrole-type Co-N_4. This result indicated that pyrrole-type Co-N_4 possessed higher 4-electrons selectivity. Therefore, a trade-off between activity and selectivity should be considered when regulating the coordinated nitrogen types.

3.2 Heteroatom substitution

One of the strategies to improve the intrinsic activity of SACs is to adjust the coordination environment of center atoms [72, 134]. In view of the difference in electron spin density and electronegativity between N and other heteroatoms (i.e., S [70], O [86], P [135], B [136]), replacing the coordinated N with heteroatoms could break the symmetrical distribution of electrons in M-N_4 and improve

ORR activity [137, 138]. For instance, Wu et al. embedded atomically dispersed Fe atoms into N and S co-doped carbon substrate and obtained N, S-coordinated Fe-N-C catalyst (denoted as Fe(Fc)-N/S-C) with Fe-N_3S_1 as active sites (Fig. 5(a)) [70]. The presence of Fe–S bond was evidenced by Fe–S characteristic peak observed at 161.8 eV in XPS spectrum, which caused a positive shift of Fe-N binding energy. Due to the electronic regulation effect, Fe(Fc)-N/S-C catalysts delivered better ORR activity ($E_{1/2}$ = 0.872 V) than Fe(Fc)-N-C (Fe-N_4 as active sites) ($E_{1/2}$ = 0.834 V) (Fig. 5(b)). Mechanistic study was performed to gain insights into the activity enhancement by S substitution. The differential charge density diagram clearly showed the electron transfer from S to Fe, resulting in higher electron density of Fe atoms in Fe-N_3S_1 site than that in Fe-N_4 (Fig. 5(c)). The regulated electronic states of Fe site promoted *OH desorption towards decreased energy barrier of RDS. In a study by Makonnen and coworkers, the substitution degree was investigated by constructing five models, including Co-N_4/C, Co-S_4/C, Co-N_2S_2/C, Co-N_2S_3/C, and Co-N_3S/C [42]. Their performance was found to follow the sequence as Co-N_4/C < Co-S_4/C < Co-N_2S_2/C < Co-N_2S_3/C < Co-N_3S/C. In this research, electron transfer from Co to N/S occurred, which would optimize the binding strength of *OH on Co-N_3S sites (Fig. 5(d)). Further introducing O into the S, N-coordinated Fe-N-C catalyst would lead to higher ORR activity. Ruan et al. rationally designed Fe-N_3OS sites via introducing sacrificial bonds [71]. DFT calculations showed that the d-band center of Fe-N_3OS further decreased compared with both Fe-N_4 and Fe-N_3S sites (Fig. 5(e)). The energy barrier of RDS was decreased from 0.58 to 0.26 eV upon O doping (Fig. 5(f)).

Apart from S, P element was selected as substitute for N to regulate the electronic configuration of metal centers. For instance, Scherf et al. designed Fe-N_3P site for ORR, and the as-prepared catalyst showed excellent ORR activity with E_{onset} and $E_{1/2}$ as 0.941 and 0.867 V, respectively [72]. Beyond that, surprising activity has also been demonstrated in ZABs with open-circuit voltage of 1.42 V and power density of 133.2 mW·cm^{-2}. The theoretical calculations verified that P could promote oxygen adsorption on Fe site and decrease energy barrier of RDS (*OH→H_2O) from 1.02 to 0.85 eV. In the study by Li and coworkers, substituting N with P was proven able to regulate the catalytic properties of Co/Ni dual-atom sites as well [135]. To be specific, the charge density differences revealed that strong electronic localization and spin polarization could be observed in Co-N_3P_1 and Ni-N_3P_1 sites, resulting in more negative valence state in M-N_3P_1 sites than that in the pristine M-N_4 sites. Such an electronic regulation facilitated the ORR process and promote the four-electron ORR pathway. Further increasing P content resulted in the formation of Co-N_2P_2 site [116], which was also verified to impel favorable oxygen

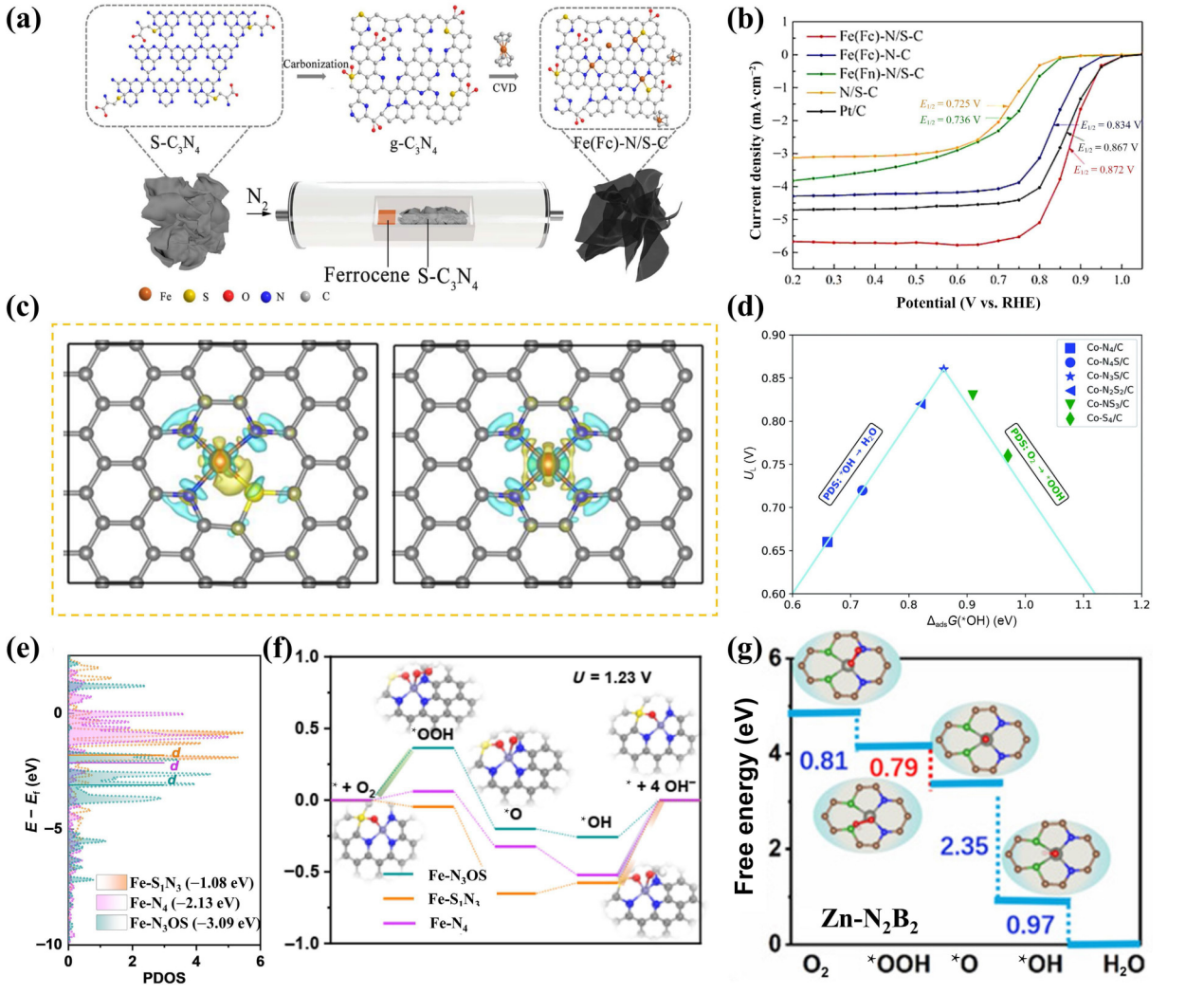

Figure 5 (a) The synthetic process of the Fe(Fc)-N/S-C catalyst. (b) The ORR performance of Fe(Fc)-N/S-C. (c) Charge density differences of Fe-N_3S (left) and Fe-N_4 (right) [70]. (d) Volcano plot for the ORR limiting potential (U_L) against the Gibbs free energy of $\Delta_{ads}G$(*OH) [42]. (e) The d-band of Fe-S_1N_3, Fe-N_4, and Fe-N_3OS referenced to the Fermi level. (f) Calculated free energy evolution of each elementary step on Fe-S_1N_3, Fe-N_4, and Fe-N_3OS sites [71]. (g) The free energy diagrams and key reaction intermediates of Zn-N_2B_2 [136]. (a)–(c) Reproduced with permission from Ref. [70], © American Chemical Society 2021. (d) Reproduced with permission from Ref. [42], © The Royal Society of Chemistry 2022. (e) and (f) Reproduced with permission from Ref. [71], © Wiley-VCH GmbH 2021. (g) Reproduced with permission from Ref. [136], © Wiley-VCH GmbH 2020.

adsorption on Co site. Besides, it could accelerate oxygen dissociation through lowering the energy barrier from 0.33 to 0.271 eV. Apart from this, engineering P, S co-coordinated sites has been proven as a feasible strategy to optimize the ORR activity. For instance, Li et al. synthesized Co_1-N_3PS sites embedded into carbon support [134]. It exhibited an ultra-high $E_{1/2}$ of 0.92 V, surpassing Co_1-N_4 catalysts and commercial Pt/C.

Beyond that, recent researches have reported that other coordinated elements, such as O and B, show promotion effect in tailoring ORR performance of M-N-C SACs. For example, Chen et al. investigated Mn-N_2O_3, Mn-N_2O_2, and Mn-N_3O_1 sites theoretically [86]. The d-band center of Mn in Mn-N_3O_1 is the lowest than those of Mn-N_2O_3 and Mn-N_2O_2. This implied that Mn-N_3O_1 presented the optimum reaction energy. Besides, Zn-N_2B_2 was designed to strengthen the adsorption of ORR intermediates on Zn site (Fig. 5(g)) [136]. Due to the weak electronegativity, B could denote electron to the nearby N atoms, resulting in electron reservation for Zn 4s and stronger binding strength with ORR intermediates.

3.3 Axial coordination

Engineering axial ligands have proved to be an effective strategy to adjust the electronic and geometric structure of M-N-C SACs [139]. For instance, Liu et al. constructed a series of iron porphyrin $FeF_{20}TPP$ (5-tetra(pentafluorophenyl) iron porphyrin) coordinated with different axial ligands on the surface of multi-walled carbon nanotubes (MWCNTs) varying from imidazole to thiophene [140]. It was found that the ORR performance could be significantly boosted via introducing above ligands, of which imidazole displayed the highest promotion effect. In view of dependence of ORR activity on the ligand type, more efforts have been devoted to clarify the potential mechanisms and exploit the optimal ligand. For example, Yu et al. employed the commercially available MCNTs with various functional groups R (R represents $-NH_2$, –OH, and –COOH) for anchoring FePc molecular [141]. These functional groups served as axil ligands coordinated with Fe site (FePc/CNT-R) (Fig. 6(a)). Their ORR activities were found highly dependent on electron-donating ability of ligand and follow the sequence as FePc/CNT–NH_2 > FePc/CNT–OH > FePc/CNT–COOH > FePc/CNT. Notably, the most electron-denoting ligand, $-NH_2$ endowed the catalyst FePc/CNT–NH_2 with highest ORR performance ($E_{1/2}$ = 0.92 V) in alkaline medium, surpassing commercial Pt/C catalyst ($E_{1/2}$ = 0.85 V) (Fig. 6(b)). DFT calculations revealed that axial coordination of the electron-donating group NH_2 promoted O_2 adsorption on Fe site. Besides, the enhance of D3 (O-Fe-N_4-O_2) content revealed axial O coordination could promote O_2 adsorption on Fe-N_4 site via ^{57}Fe Mössbauer spectroscopy [75].

In addition to promote O_2 adsorption, axial ligand has been proven to optimize the binding strength with *OH on M-N-C SACs. For instance, Xing et al. revealed the promotion effect of axial OH ligands on Ru-N_4 site via DFT calculations [95]. The electron-withdrawing OH ligand caused electron transfer from Ru, thus downshifting the d-band center from −2.03 to −3.22 eV. Therefore, the last electron transfer step, *OH desorption, would be accelerated on the Ru-N_4-OH site and led to higher ORR activity. The effect of axial OH ligand was found dependent on the active site configurations. Using poly(iron phthalocyanine) (PFePc) as Fe-N_4-based model catalysts, Sun et al. investigated the ligand effect on the catalytic performance of Fe-N_4 site, where strong-field ligand, –NCS and weak-field ligand, i.e., –OH, –I were systematically studied [142]. The Fe 3d orbital energy level changed significantly after the axial coordination and it was found that the energy level of d_{z^2} decreased as the field strength of the axial ligands decreased (Fig. 6(c)). The decreased d_{z^2} energy level suggested easier *OH desorption since *OH desorption process was accompanied by electron transfer from Fe d_{z^2} to OH p_x/p_y orbitals (Fig. 6(d)). On this basis, PFePc–OH with the lower d_{z^2} energy level exhibited the higher ORR performance than PFePc–I and PFePc–NCS. In view of this, the crystal field strength of the ligand should be taken into consideration when designing M-N_4 with axial-ligand. Besides, the axial ligand could regulate the spin state of Fe site towards improved activity. For instance, Wang et al. introduced -O-Ti ligand to the Fe-N-C catalyst and found a low-to-medium spin state transition (Fig. 6(e)) [143]. The modulated spin state was beneficial for oxygen adsorption, as evidenced by a more negative value of integrated-crystal orbital Hamilton population (ICOHP) on FeN_3O-O-Ti site (−1.88 vs. −1.65 on FeN_3O site) (Fig. 6(f)). As a result, the *OOH formation process was obviously accelerated on the FeN_3O-O-Ti site (Fig. 6(g)). In spite considerable activity improvement achieved by axial ligand coordination, the stability of these ligands under working condition should be considered in future study.

4 Heteroatom doping

As the M–N_x active site is embedded into the carbon substrate, the long-range electronic effect between surrounding carbon support and M–N_x site would affect the catalytic properties as well. For example, non-metallic heteroatoms such as sulfur [144–146], phosphorus [147], fluorine [148], etc. can be effectively introduced into the carbon plane to moderate the electronic and geometric structures of SACs for boosted activity.

4.1 Sulfur doping

Compared with N atom, S atom owns larger atomic radius and smaller electronegativity [149], which could break the symmetry of carbon six-membered ring and adjust the local electronic structure of M-N_4 site when doped into the carbon plane. Besides, S doping was reported able to enlarge the surface area of carbon supports thus promoting the accessibility of reactants during the ORR reaction. For instance, Lv and coworkers reported that the specific surface area of Fe/SNCFs-NH_3 catalyst increases from 904 to 1092 $m^2 \cdot g^{-1}$ via S-doping, which could provide high content of accessible Fe-N_4 sites and promote the accessibility of reactants during the ORR reaction [150]. The ORR performance of Fe/SNCFs-NH_3 catalyst ($E_{1/2}$ = 0.89 V) was higher than that of S-free Fe/NCFs-NH_3 catalysts ($E_{1/2}$ = 0.86 V) and commercial Pt/C ($E_{1/2}$ = 0.86 V). Besides, the open-circuit voltage and peak power density of ZABs with Fe/SNCFs-NH_3 as cathode were 1.38 V and 255.84 $mW \cdot cm^{-2}$, respectively. These experimental results revealed that enhancing the surface area of M-N-C single atom catalyst via S-doping can be an efficient strategy to optimize the ORR performance. Additionally, S doping could induce the transition of spin polarization configuration. Increased content of low spin Fe^{3+} (D1) was detected on the S-doped Fe-N-C catalyst (58%) [151], while only 28.8% of D1 was observed on the undoped Fe-N-C sample. Further increasing S dopants led to a decrease of D1 (40%). This illustrated that moderate S doping will promote the formation of high active sites, thus enhancing the ORR activity by promoting the formation of the high ORR active site.

Besides, it should be noted that the configuration of S dopants would exert different effects. For instance, Lee et al. adjusted the S species, i.e., thiophene-like S (C-S-C) and oxidized S (C-SO_x) by controlling the content of S precursor, dibenzyl disulfide (DBDS) (Fig. 7(a)) [152]. The catalyst dominated by C-SO_x and C-S-C is denoted as FeNC-S-MSUFC-2 and FeNC-S-MSUFC-4, respectively. Interestingly, FeNC-S-MSUFC-2 outperformed FeNC-S-MSUFC-4 by showing a more positive $E_{1/2}$, indicating that it is C-SO_x which could boost the intrinsic activity of Fe-N_4

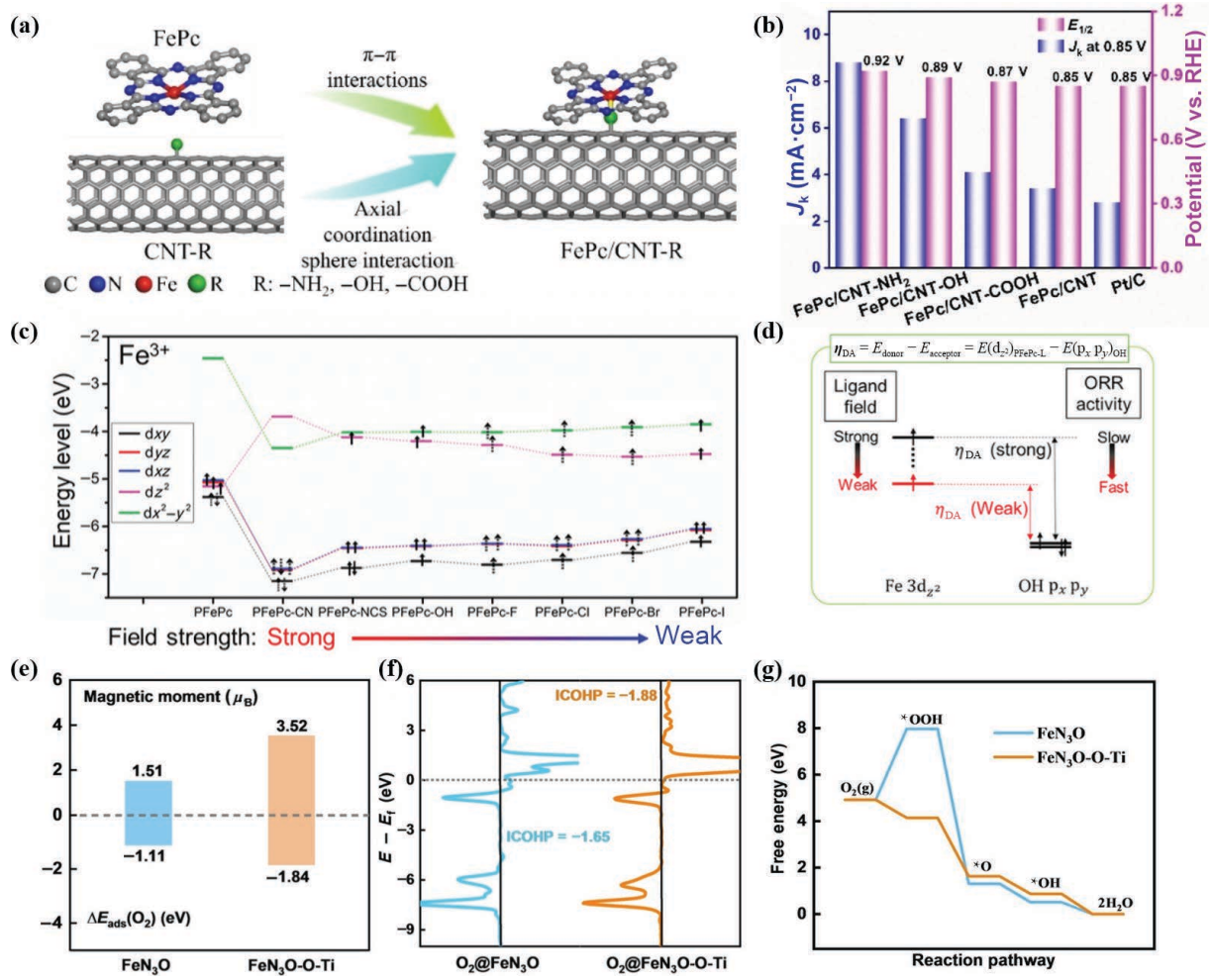

Figure 6 (a) The synthesis process of FePc/CNT-R. (b) The ORR performance of FePc/CNT-R [141]. (c) Calculated Fe 3d orbital energy levels of PFePc and PFePc-L and the electron configurations. (d) Intermolecular hardness (η_{DA}) between PFePc-L and *OH [142]. (e) Calculated relationship between magnetic moment (μ_B) and $\Delta E_{ads}(O_2)$ of FeN_3O and FeN_3O-O-Ti. (f) Integrated-crystal orbital Hamilton population (ICOHP) between O_2 species and FeN_3O and FeN_3O-O-Ti. (g) The free energy changes for ORR on FeN_3O and FeN_3O-O-Ti [143]. (a) and (b) Reproduced with permission from Ref. [141], © Wiley-VCH GmbH 2021. (c) and (d) Reproduced with permission from Ref. [142], © Wiley-VCH GmbH 2022. (e)–(g) Reproduced with permission from Ref. [143], © Wiley-VCH GmbH 2022.

site (Fig. 7(a)). A contradictory conclusion was achieved by Guo and co-workers [153]. They proposed C-S-C as a promotor for Fe-N_4 site, which is able to reduce electron localization around Fe atom and optimize the interaction between Fe-N_4 site and ORR intermediate. Besides, the distance between Fe-N_4 and C-S-C was considered in their study, revealing that the beneficial effect only occurred when the distance was about 7.3 Å (Fig. 7(b)). In line with this hypothesis, Mu et al. considered that C-S-C shifted the d-band center of Fe close to the Fermi energy and benefited the oxygen adsorption [154]. Similarly, Wang et al. demonstrated that the 3d orbital configuration of Co could be optimized by S doping towards easier oxygen adsorption [155]. Unlike the above-mentioned mechanisms, Xu et al. proposed that S doping led to spatial repulsion interaction with the ORR intermediates on Mn-N_4 site, thus weakening their adsorption and facilitating the desorption process, which enhance the stability of Mn-N-C-S catalysts (Fig. 7(c)) [81].

4.2 Phosphorus doping

Due to the lower electronegativity of phosphorus (P), P-doping can adjust the electronic structure of the carrier through electron donating effect and induce the formation of defect sites. A recent research has proved that the synergistic effect between doped P atoms substrates and Fe-N_x sites can effectively promote the ORR process [156]. Using a sacrificial template method, Zhang et al. prepared P doped Fe-N-C catalyst (Fe-N-C-P/N,P-C) [55], which exhibited appealing ORR performance with $E_{1/2}$ of 0.80 V in 0.1 M $HClO_4$ solution (Fig. 8(a)). P doping was believed to drive the electron delocalization and decrease the bad gap of Fe-N_4 site, thereby weakening the free energy barrier of four-electron ORR process. In the study by Shao and co-workers, they investigated the configurations with P doped into the second shell around Fe-N_4 sites [157]. The P-doped sites demonstrated lower theoretical overpotentials of 0.75 V than that of pristine Fe-N_4 site (0.77 V). In addition, the thermodynamic overpotential of Fe-N_4 and P-doped Fe-N_4 was estimated to be 0.34 and 0.32 eV, respectively, in RDS (*OH-H_2O). These results strongly confirm the promotion effect of P doping on the ORR activity enhancement. As P is easily bonded with O, Fe-N_4 with a P–O bond was proposed by Yan and co-workers [158]. The incorporation of P–O groups altered the charge density distribution and electronic structure of Fe sites, thus promoting the *OH desorption process. It should be noted that P–O doped Fe-N_4 site was demonstrated more active than the P-doped Fe-N_4 site. Above experimental and theoretical results confirm P-doping can effectively improve the ORR activity of M-N_4 sites. However, the configuration P-doping can't be precisely controlled because the conventional synthetic procedure involves high temperature pyrolysis. Therefore, it is difficult to identify the authentic promotion mechanism via physical characterization. On this basis, it is urgently desirable to develop new strategies towards controllable P-doping.

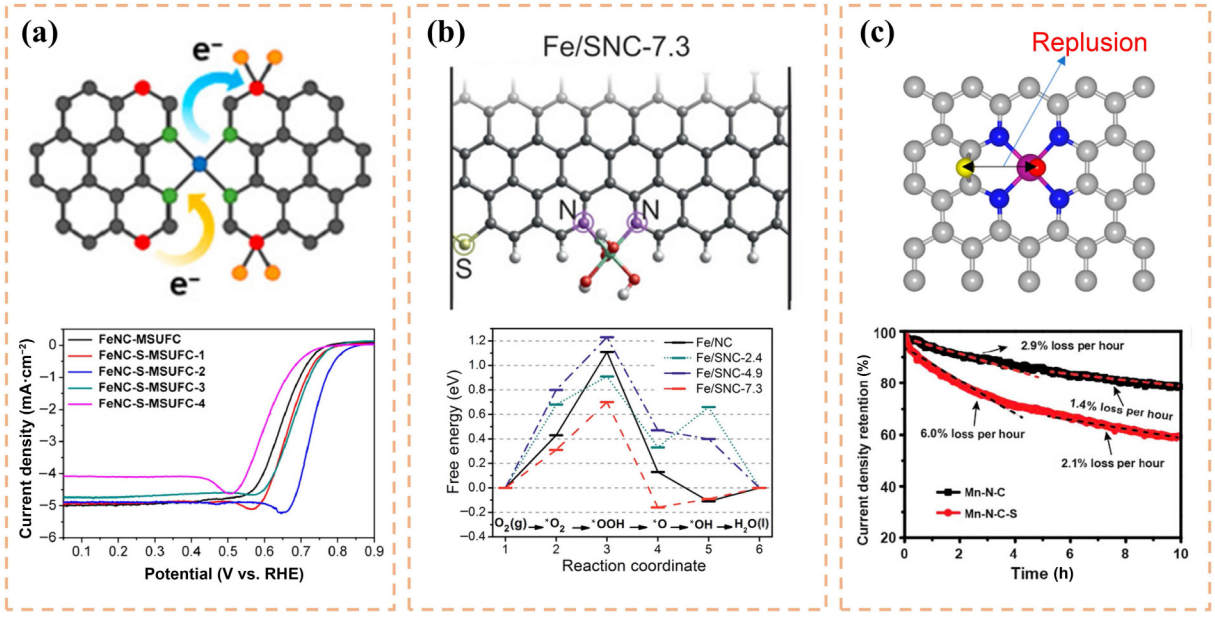

Figure 7 (a) The schematic diagram of oxidized S/thiophene S doping (up) and the ORR performance of FeNC-S-MSUFC-2 (down) [152]. (b) The structure of Fe/SNC-7.3 (up) and free energy diagram for the Fe/NC and Fe/SNC systems of U = 1. 23 V [153]. (c) The structure of C–S–C near to Mn-N_4 sites (up) and the stability of Mn-N-C-S catalysts (down) [81]. (a) Reproduced with permission from Ref. [152], © American Chemical Society 2019. (b) Reproduced with permission from Ref. [153], © Wiley-VCH Verlag GmbH & Co. KGaA, Weinheim 2017. (c) Reproduced with permission from Ref. [81], © American Chemical Society 2021.

4.3 Fluorine doping

As the most electronegative element, Fluorine (F) has been employed to optimize the ORR activity of metal sites. For instance, Li et al. reported F-doped Fe-N-C catalysts using Fe-zeolitic imidazolate framework-8 (Fe-ZIF-8) and ammonium fluoride as precursors [159]. In this work, they found F-doping could increase the content of pyridinic-N and pyrrolic-N, thus facilitating Fe-N_4 site formation. Besides, the doping of F breaks the electric neutrality of carbon support and synergistically promotes the ORR activity of Fe-N_4 site. The beneficial effect of F-doping on promoting the formation of pyridinic-N and pyrrolic-N was also evidenced in a report by Ahn and co-workers [160]. In Müllen et al.'s work, the effect of F doping was clarified as enlarged surface area, increased active sites (higher content of D1 and D3, Fig. 8(b)), and strong electron-withdrawing effect [161]. These merits endow the F-doped Fe-N-C catalyst with a 30 mV positive shift in $E_{1/2}$ compared with the Fe-N-C. Theoretical calculations reveal that F doping could balance the *OH adsorption on the Fe site that it is neither too strong nor too weak. More interestingly, F-doped Fe-N-C catalyst showed excellent stability with only 13 mV loss in $E_{1/2}$ after 60,000 cycles of accelerated stress tests (ASTs) (Fig. 8(b)).

Although F-doping has been proven effective to boost the ORR performance, there remain some challenges. First, the content of the F is relatively low, how to increase the dopant content and investigate its effect on ORR activity is highly desirable. Secondly, the optimal coordination configuration of F with respect to Fe-N_4 site needs to be reasonable designed.

4.4 Boron doping

The electronegativity of Boron (B) is merely 2.02 less than C (2.55) and presents an electron-deficient state. So, B-doping is enough to adjust the charge density on the carbon plane and enhance the ORR activity. For instance, Liu et al. doped B into Fe-N-C (Fe-N_4-C-B-900) catalyst through a high temperature pyrolysis and confirmed that B-doping positively shift $E_{1/2}$ by 24 mV compared with the pristine Fe-N-C catalyst [162]. Besides, Fe-N_4-C-B-900 displayed superior stability to the Pt/C benchmark, retaining 93% of the initial current after 25 h of operation at 0.65 V. This work has proved that the synergistic effect between B and Fe-N_4 site could effectively improve ORR activity and stability. In addition to this, Hu et al. prepared B-doped Fe-N-C catalyst (Fe-N_4-C-B) by the impregnation method with *closo*-$[B_{12}H_{12}]^{2-}$, 1,10-phenanthroline-iron and ZIF-8 as precursor [163]. The Fe-N_4-C-B catalysts presented lower Tafel slope (85.41 mV·dec^{-1}) than Fe-N_4 (141.40 mV·dec^{-1}), which demonstrated that B-doping improved the ORR activity of Fe-N_4 sites (Fig. 8(c)). To uncover the mechanism B-doping, DFT calculations were conducted. The lower d-band center of Fe-N_4-C-B implied a weakened O_2 adsorption induced by B-doping. Thus, the bond length of adsorbed O_2 was extended from 1.48 Å (Fe-N_4-C) to 2.03 Å (Fe-N_4-C-B), leading to the easier O–O bond breaking. What's more, the Fe–O bond was found to increase from 1.884 Å (Fe-N_4-C) to 1.925 Å (Fe-N_4-C-B), resulting in decreased dissociation energy barrier towards 4-electron ORR pathway. Whereas in another study, B-doping was regarded to enhance oxygen adsorption on Fe site by transferring electron from N to B [164]. The reduced interaction between Fe-3d and N-2p orbital was responsible for the enhanced ORR performance. The doping level and configuration were further investigated in a theoretical study [165]. It was revealed that B-doping could lower the charge density of Mn site, therefore weakening the adsorption energy of ORR intermediates towards higher ORR activity. The optimal structure, Mn-N_4-B_4 exhibited high onset potential for ORR (U_{onset} = 0.84 V and ΔG_{*OH} = 0.96 eV). Another insight into the effect of B has been proposed by Ullrich Scherf [166]. Specifically, B atom was regarded as additional sites for O_2 molecule adsorption based on DFT calculations, which can symmetrically accelerate ORR kinetics with Fe-N_4 sites. The B–O bond (2.157 Å) has also been confirmed to be longer than Fe–O bond in Fe-N_4-B_2 in Fig. 8(c), demonstrating that the first step of ORR process should occur at B@Fe-N_4-B_2 sites more easily.

4.5 Other heteroatom doping

In addition to those elements summarized above, other elements have also been reported for their specific properties. For example, Zhai and coworkers doped Se into Fe-N-C catalyst (Fe_1Se_1-NC) for ORR [167]. The ORR performance of Fe_1Se_1-NC catalysts ($E_{1/2}$

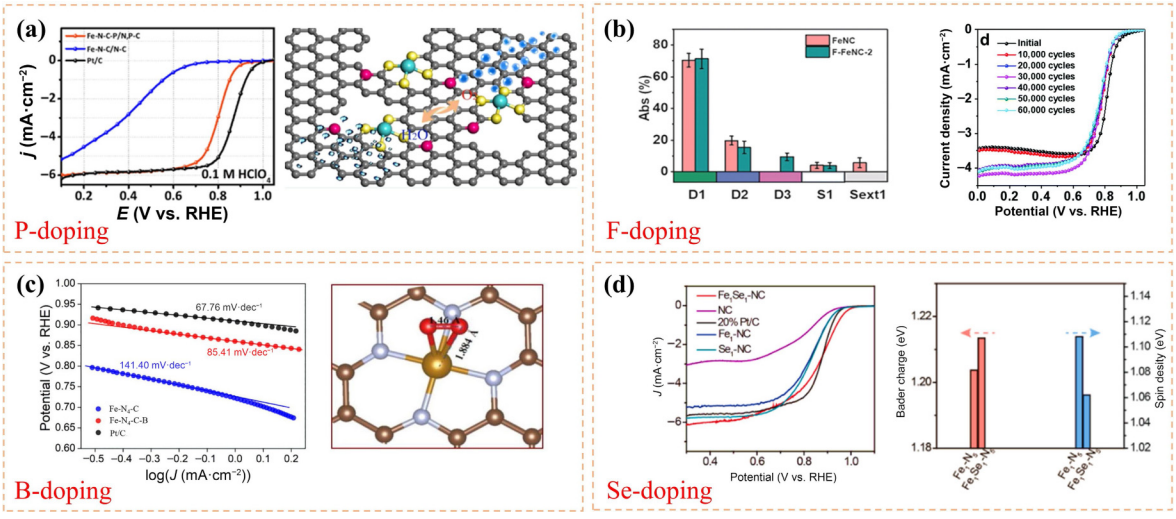

Figure 8 (a) The ORR performance and structure of P-doping [55]. (b) Different components of Fe species of F-doping and durability tests by cycling the potential of F-doped Fe-N-C in O_2-saturated 0.5 M H_2SO_4 [161]. (c) Tafel plots converted from LSV signals of Fe-N_4-C, Fe-N_4-C-B, and Pt/C (left) and optimized geometry structure of O_2 adsorption for the Fe-N_4-C-B (right) [163]. (d) The ORR performance, Bader charge, and spin density value of Fe_1Se_1-NC and Fe_1-NC [167]. (a) Reproduced with permission from Ref. [55], © American Chemical Society 2021. (b) Reproduced with permission from Ref. [161], © The Royal Society of Chemistry 2022. (c) Reproduced with permission from Ref. [163], © Science Press and Dalian Institute of Chemical Physics, Chinese Academy of Sciences. Published by ELSEVIER B.V. and Science Press 2022. (d) Reproduced with permission from Ref. [167], © Elsevier B.V. 2022.

= 0.88 V) was better than those of Fe_1-NC ($E_{1/2}$ = 0.84 V) and Se_1-NC catalysts ($E_{1/2}$ = 0.85 V) (Fig. 8(d)). The synergistic effect could be attributed to the following points. First, the volatilization of SeO_2 during pyrolysis process would result in the formation of porous structure of Fe_1Se_1-N-C catalyst, which was conducive to mass transfer in ORR process. Second, Se-doping increased the content of low spin component Fe^{3+} (D_3) of Fe_1Se_1-N-C catalyst, beneficial for enhancing the ORR activity. Last, DFT calculations demonstrated that Se-doping enabled an appropriate Bader charge and spin density, thus weakening the adsorption and facilitating the four-electron process (Fig. 8(d)). In addition to this, O-doping was revealed to promote the ORR process [168]. The increased content of mesopores and surface hydrophilicity was proposed to contribute to the activity improvement. Besides, DFT calculation demonstrated that O-doping promoted the *OOH formation and *OH desorption, reducing the energy barrier of the RDS.

4.6 Multiple heteroatom regulation

Except for the single regulation strategy, regulation of coordinated atoms and heteroatoms doping simultaneously has been adopted to regulate ORR properties. For instance, Li and coworkers loaded single Fe sites on the P, S co-doped hollow carbon polyhedron (denoted as Fe-SAs/NPS-HC) successfully [169]. Such a synergistic effect between P/S and Fe-N_4 sites endowed Fe-SAs/NPS-HC catalysts with better ORR activity ($E_{1/2}$ = 0.912 V, J_k = 71.9 mA·cm^{-2} at 0.85 V) than Pt/C catalysts ($E_{1/2}$ = 0.840 V, J_k = 4.78 mA·cm^{-2} at 0.85 V). The DFT calculations revealed that P, S co-doping could donate electrons to Fe sites, which could weaken the binding strength with *OH towards higher intrinsic ORR activity. Besides, a typical representative study was reported by Li et al. in 2018 [170]. In this study, they combined Cl atom axial ligand coordination with S doping to boost the ORR performance. It was found that the long-range interaction of S could lead to the negative shift of d-band center and narrow gap towards Fermi level of Fe sites. Besides, the near-range interaction with Cl could further optimize the O_2 binding energy. Thanks to the Cl and S co-doping, $FeCl_1N_4$ sites would become closer to the apex of the volcano curve than Fe-N_4 sites. Similarly, S and B co-doping strategy was applied to adjust the electronic structure of p-block metal single atom catalysts towards higher selectivity [171]. In such a catalyst, S was directly coordinated with central indium (In) atom, while B was doped into the second coordination shell. They cooperated well to optimize the charge localization of In center for a moderate binding energy of ORR intermediates. These exhibited merits of multiple heteroatoms doping strategy further boost ORR performance of M-N-C SACs. Despite these achievements, increasing efforts should be devoted to unveil more insights into regulatory mechanisms in multiple heteroatom doping.

Heteroatom doping could make great contribution to the performance of the catalysts via synergy effect and electronic structure optimization. To precisely clarify the underlying mechanism of the heteroatomic doping, controllable synthetic methods to regulate the doping degree and configuration are required.

5 Defect engineering

As the catalytic performance is co-determined by the properties of M–N_x sites and the surrounding carbon substrate, defect engineering is considered as effective approach to tailor the catalytic performance of M-N-C SACs [44]. For instance, Chen and co-workers synthesized defective Fe-N-C catalyst with abundant Fe-N_4 sites located at the edge of micropores/mesopores [52], and confirmed the extraordinary intrinsic activity of edge-type Fe-N_4 site, compared with plane-type sites. Following this study, a variety of strategies have been developed to selectively fabricate defective Fe-N-C catalysts. For example, Zhao et al. reported the KOH activation strategy to create abundant defects/vacancies in carbon nanospheres followed by anchoring transition metal monomers onto the surface [172]. Initiated by theoretical prediction, Chen et al. put forward a self-sacrificed template method to prepare Fe-N-C catalyst containing abundant edge-type Fe-N_4 sites (Fig. 9(a)) [62]. In their study, excessive Fe precursor was introduced to serve as sacrificed template for the preferential deposition of edge-type sites. DFT calculations revealed that more charge transfer from the Fe atom to the N atom could be observed at edge-type Fe-N_4 (1.17e$^-$), compared with plane-type Fe-N_4 (0.97e$^-$). This suggested a weaker adsorption strength of ORR intermediate on the edge-type Fe-N_4 site. Gibbs free energy diagram further confirmed that the decreased binding strength with *OH contributed to the improved ORR performance of edge-type Fe-N_4 site. In the study of Yao et

al., the defect content can be regulated by controlling the content of $FeCl_3$ [44]. Increasing the $FeCl_3$ content from 40 to 60 mg could lead to the formation of more defects, whereas further raising its content to 80 mg, the pore was fused into a large pore and led to some degree of structural collapse. The electrochemical tests showed that the catalyst using 60 mg $FeCl_3$ as precursors (Fe-N_4-C-60) exhibited the highest ORR activity, highlighting the importance of defect size and content. In addition to the above-mentioned template strategy, other facial methods have been exploited as well. For instance, Wang et al. reported a selective C–N bond cleavage approach to Fe-N-C catalyst with edge-type Fe-N_4 sites, which was accomplished by porosity engineering via a pyrolysis process [173]. In their study, the crucial role of defect content and position was investigated by theoretical calculations.

Besides, Wang et al. engineered defects by the pyrolysis of carboxylate/amide mixed with ligand zinc MOF (DMOF) [174]. They found a linear relationship between ORR performance and defect contents. By carrying out DFT calculations, the. configuration of the defective site was proposed as Co-N_4-6r-c2 (Fig. 9(b)), similar as the structure reported by Wang et al [173]. This unique structure could enhance oxygen adsorption on Co site for a faster ORR kinetic (Fig. 9(c)). In future research, methods to raise the defect content and control the configuration precisely would become the research hot spot.

6 Synergistic effects between nanoparticles and SACs

Although great efforts have been made to improve the performance of the SACs, it is still difficult to meet the demand for practical application due to the unsatisfied stability and activity. Aiming at promoting the intrinsic activity and extending stability, the introduction of nanoparticles (NPs) has been adopted to corporate with the M-N_4 sites [156, 175–179]. For example, Feng and his coworkers incorporated Co NPs into Fe-N-C catalyst (Co@Fe-N-C) to tailor the properties of Fe-N_4 sites [45]. As expected, the Co@Fe-N-C performed superior ORR performance ($E_{1/2}$ = 0.92 V) to Fe-N-C catalyst ($E_{1/2}$ = 0.85 V) (Fig. 10(a)). Besides, Co NPs were proven capable of enhancing the catalytic performance of Co-N_4 sites as well. By introducing Co NPs, the Co-N-C catalyst developed by Yang's group demonstrated an impressive ORR performance with $E_{1/2}$ of 0.778 V in acidic solution [180]. In order to unveil the synergetic effect between Co NPs and Co-N_4 sites, Lu and co-workers employed DFT calculations [181]. Besides, they investigated the size effect of Co NPs by constructing two different models (Co-N_4@Co_{12} represents small Co NPs; Co-N_4@Co_{2layer} represents large Co NPs, as shown in Figs. 10(b) and 10(c)). The results confirmed that the incorporation of Co NPs irrelative with particle size would weaken oxygen adsorption on Co-N_4 site, with a moderate binding strength on the Co-N_4@Co_{12} surface. The beneficial effect of atomic clusters on M–N_x sites were certified by Zeng and co-workers [182]. Four different models including Fe_1@Fe_{SA}-N-C, Fe_{13}@Fe_{SA}-N-C, Fe_{NP}@Fe_{SA}-N-C, and Fe_{SA}-N-C were built. In contrary to the conclusion of Co-N-C, only atomic Fe clusters improved the ORR activity of Fe-N_4, while large NPs decreased the ORR performance by strengthening the oxygen adsorption on Fe site (Figs. 10(d) and 10(e)). A similar result was achieved in a research by Peng's group [183]. The charge density difference analyses revealed small-size Fe clusters could induce electron redistribution around Fe-N_4 sites. The decreased electron density of Fe center weakened the adsorption of *OH. In sharp contrast, the large-size Fe NPs would denote electron to Fe-N_4 site, resulting in enhanced *OH adsorption. Apart from the metals, metal compounds (i.e., Fe_2N [176], Fe_3C [184]) were adopted to boost the ORR performance of M–N_x sites through negatively shifting the d-band center away from Fermi level. In a recent report, the introduction of Co NPs was found able to improve the catalytic stability of Co-N-C [185]. The as-designed catalyst (*d*-Co_{NP}/Co_{SA}-N-C) exhibited excellent stability with a 12 mV negative shift of $E_{1/2}$ after 50 K cycles (0.6–1.0 V) in acidic solution. DFT calculations revealed that the introduction of Co_4 to Co-N_4 could enhance the OOH adsorption and weaken the O–O bond, resulting in easier cleavage of O–O bond than Co-N_4. Thus, the formation of H_2O_2 could be inhibited for improved stability. The promotion effect of NPs in activity and stability has been demonstrated. However, the electrochemical stability of NPs in strong acidic condition should be seriously considered. Besides, rational construction of the synergetic structure is still a challenge and deserves more effort to achieve the ideal performance.

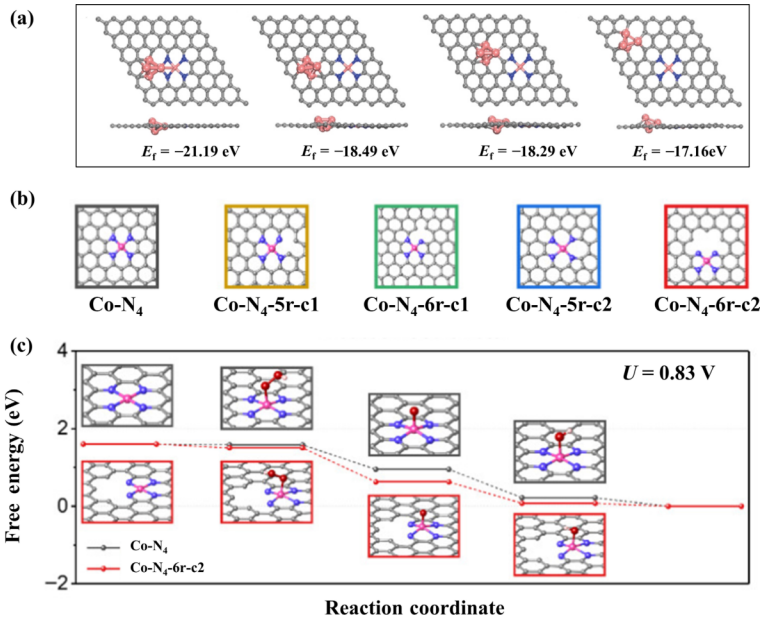

Figure 9 (a) Various Fe cluster/Fe-N_4 site configurations and the corresponding formation energy (E_f) [62]. (b) The five possible models of atomic Co-N_4 configurations with different defective degrees. (c) Free energy diagrams of above models were calculated at U = 0.83 V [174]. (a) Reproduced with permission from Ref. [62], © Wiley-VCH GmbH 2020. (b) and (c) Reproduced with permission from Ref. [174], © Wiley-VCH GmbH 2021.

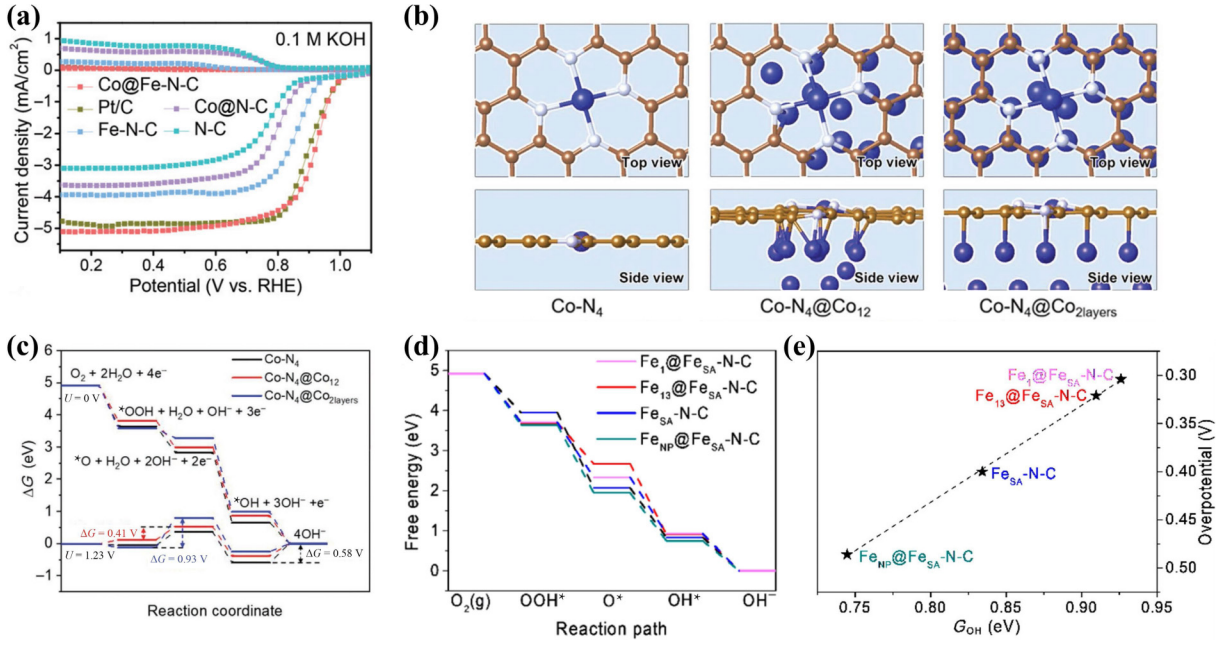

Figure 10 (a) LSV curves of Co@Fe-N-C, Fe-N-C, and Co@N-C [45]. (b) Top views (upper panels) and side views (bottom panels) of Co-N_4, Co-N_4@Co_{12}, and Co-N_4@$Co_{2layers}$. (c) ORR free energy diagrams for Co-N_4, Co-N_4@Co_{12}, and Co-N_4@$Co_{2layers}$ at U = 0 and 1.23 V [181]. (d) Free energy diagram of ORR for Fe_1@Fe_{SA}-N-C, Fe_{13}@Fe_{SA}-N-C, Fe_{NP}@Fe_{SA}-N-C, and Fe_{SA}-N-C. (e) Calculated overpotentials of the ORR for the Fe_1@Fe_{SA}-N-C, Fe_{13}@Fe_{SA}-N-C, Fe_{NP}@Fe_{SA}-N-C, and Fe_{SA}-N-C models [182]. (a) Reproduced with permission from Ref. [45], © The Royal Society of Chemistry 2021. (b) and (c) Reproduced with permission from Ref. [181], © Wiley-VCH GmbH 2021. (d) and (e) Reproduced with permission from Ref. [182], © American Chemical Society 2019.

7 Summary and perspective

Due to their cost effectiveness, defined active site structure, and tunable catalytic performance, M-N-C SACs have been hailed as promising alternatives to the expensive Pt-based catalysts for ORR. Further improvement in their intrinsic activity is essential to rival the state-of-the-art Pt benchmarks, necessitating the rational design of catalyst structure. Since the activity is determined by the electronic states of the central metal atom, proper regulation of the microenvironment surrounding metal atoms is an appealing approach. This review summarizes the recent progress in the microenvironment regulation of M-N-C SACs towards enhanced ORR performance regarding coordination environment regulation, heteroatom doping, defect engineering, and synergic site construction. Combining the theoretical calculations and experimental results, we attempt to gain a coherent picture of the structure–function relationship between the coordination structure and catalytic properties. Despite significant progress made in terms of mechanism comprehension and performance improvement, some essential issues remain to be urgently addressed.

(1) Most of the synthetic methods reported in the literature are based on high temperature pyrolysis. To surpass the Ostwald ripening under high temperature, limited metal content is always a prerequisite for the preparation of prepare-N-C SACs catalysts, leading to low active site density. Moreover, the conventional high temperature annealing strategy would cause uncontrollable active site structure, i.e., co-existence of pyridinic N- and pyrrolic N-coordinated sites. Therefore, innovative synthetic strategies are urgently desirable for the preparation of high metal loading and uniform structure M-N-C SACs.

(2) Stability is one of the bottlenecks for the practical application of M-N-C SACs, especially under harsh electrochemical conditions of PEMFC. The origin of the initial activity loss has always been a controversial issue, with various degradation mechanism proposed. For instance, demetallation of M–N_x sites would not only cause a loss in active site number, but also initiate Fenton reactions to generate poisoning oxygen-containing free radicals, which in turn attacks the membrane/ionomers and carbon support. In addition, micropore flooding would cause the mass transfer issues and demetallation of M-N-C SACs during practical fuel cell. Thus, developing optimized strategies (i.e., strengthening the M–N bond, increasing graphitic degree, and introducing radical scavengers) to improve stability is urgent. What's more, monitoring the dynamic structure evolution during the ORR process via advanced *in-situ* and *operando* experiments is important to elucidate the degradation mechanism, which can provide effective guidance for the rational regulation of M-N-C SACs.

(3) The active site structure is commonly identified by XAFS spectroscopy and DFT calculations. However, disparity remains between actual active site structure and the modeling result. For example, simplified single-layer graphene supercell is always employed for the modeling study, whereas the real catalyst consists of several carbon layers. Besides, distinguishing light atoms, i.e., O, N from the XAFS spectroscopy is difficult. These disparities result in different understandings on the structure–activity relationship even based on the similar structure. Therefore, more efforts need to be directed towards the development of more advanced *ex-situ* and *in-situ* characterization tools with high resolution to probe the precise structure.

(4) The first-gate screening of newly developed ORR catalysts is commonly realized using a laboratory three-electrode system, which is totally different from the practical application environment. Most M-N-C SACs perform well in the three-electrode system, but fail in the fuel cells. How to transfer the activity of M-N-C SACs to the high-performance electrode in fuel cells depends on the rational electrode design from the perspectives of optimal three-phase interfaces for mass and charge transportation. For instance, the ink formula, ionomer content, casting procedure, hot-pressing temperature/pressure, etc., are important for expressing the activity in the fuel cells. Equal attention should be paid on the electrode design and the catalyst innovation.

(5) For promoting the further development of PEMFCs and

ZABs, several factors relative to catalytic engineering should also be emphasized. Firstly, the metal mass loading is of significant importance as the high metal loading means decreased carbon content and increased active site density, which would result in a thinner catalytic layer and better mass transfer efficiency. Besides, it was established that the large BET surface area of SACs is beneficial to anchor high density M–N_x sites. What's more, the uniform dispersion of supported M–N_x sites means high-efficiency selectivity of catalytic transformations. Therefore, it is necessary to further optimize the PEMFCs/ZABs performance by tuning the uniform dispersion level of M–N_x sites. Last but not least, hierarchically porous structure can facilitate mass transport and ensure sufficient active site density simultaneously. Thus, to improve the activity and durability of SACs, more efforts should be devoted to the regulation of catalytic morphological structure.

Acknowledgements

This work was supported by the National Natural Science Foundation of China (No. 22272161).

References

[1] Pei, Y. F.; Song, H. Q.; Liu, Y.; Cheng, Y. J.; Li, W. D.; Chen, Y. M.; Fan, Y. P.; Liu, B. Z.; Lu, S. Y. Boron-nitrogen-doped carbon dots on multi-walled carbon nanotubes for efficient electrocatalysis of oxygen reduction reactions. *J. Colloid Interface Sci.* **2021**, *600*, 865–871.

[2] Wu, X.; Meng, G.; Liu, W. X.; Li, T.; Yang, Q.; Sun, X. M.; Liu, J. F. Metal-organic framework-derived, Zn-doped porous carbon polyhedra with enhanced activity as bifunctional catalysts for rechargeable zinc-air batteries. *Nano Res.* **2018**, *11*, 163–173.

[3] Liu, Z. H.; Du, Y.; Yu, R. H.; Zheng, M. B.; Hu, R.; Wu, J. S.; Xia, Y. Y.; Zhuang, Z. C.; Wang, D. S. Tuning mass transport in electrocatalysis down to Sub-5nm through nanoscale grade separation. *Angew. Chem., Int. Ed.* **2022**, *62*, e202212653.

[4] Cheng, Q. Q.; Yang, S.; Fu, C. H.; Zou, L. L.; Zou, Z. Q.; Jiang, Z.; Zhang, J. L.; Yang, H. High-loaded sub-6 nm Pt_1Co_1 intermetallic compounds with highly efficient performance expression in PEMFCs. *Energy Environ. Sci.* **2022**, *15*, 278–286.

[5] Li, Y. H.; Qu, Y. J.; Liu, C. C.; Cui, J. D.; Xu, K.; Li, Y.; Shen, H. Y.; Lu, Z. G.; Pan, H.; Xu, T. et al. Processing agricultural cornstalks toward high-efficient stable bifunctional ORR/OER electrocatalysts. *Adv. Sustainable Syst.* **2021**, *6*, 2100343.

[6] Zhuang, Z. C.; Li, Y. H.; Yu, R. H.; Xia, L. X.; Yang, J. R.; Lang, Z. Q.; Zhu, J. X.; Huang, J. Z.; Wang, J. O.; Wang, Y. et al. Reversely trapping atoms from a perovskite surface for high-performance and durable fuel cell cathodes. *Nat. Catal.* **2022**, *5*, 300–310.

[7] Zhuang, Z, C.; Li, Y.; Li, Y, H.; Huang, J. Z.; Wei, B.; Sun, R.; Ren, Y. J.; Ding, J.; Zhu, J. X.; Lang, Z. Q. et al. Atomically dispersed nonmagnetic electron traps improve oxygen reduction activity of perovskite oxides. *Energy Environ. Sci.* **2021**, *14*, 1016–1028.

[8] Yang, Q.; Xiao, Z. C.; Kong, D. B.; Zhang, T. L.; Duan, X. G.; Zhou, S. K.; Niu, Y.; Shen, Y. D.; Sun, H. Q.; Wang, S. B. et al. New insight to the role of edges and heteroatoms in nanocarbons for oxygen reduction reaction. *Nano Energy* **2019**, *66*, 104096.

[9] Zhao, S.; Yan, L. T.; Luo, H. M.; Mustain, W.; Xu, H. Recent progress and perspectives of bifunctional oxygen reduction/evolution catalyst development for regenerative anion exchange membrane fuel cells. *Nano Energy* **2018**, *47*, 172–198.

[10] Wang, L. G.; Wang, D. S.; Li, Y. D. Single-atom catalysis for carbon neutrality. *Carbon Energy* **2022**, *4*, 1021–1079.

[11] Gong, K. P.; Du, F.; Xia, Z. H.; Durstock, M.; Dai, L. M. Nitrogen-doped carbon nanotube arrays with high electrocatalytic activity for oxygen reduction. *Science* **2009**, *323*, 760–764.

[12] Mehmood, A.; Gong, M. J.; Jaouen, F.; Roy, A.; Zitolo, A.; Khan, A.; Sougrati, M. T.; Primbs, M.; Bonastre, A. M.; Fongalland, D. et al. High loading of single atomic iron sites in Fe-N-C oxygen reduction catalysts for proton exchange membrane fuel cells. *Nat. Catal.* **2022**, *5*, 311–323.

[13] Zhang, Z. Y.; Tan, Y. Y.; Zeng, T.; Yu, L. Y.; Chen, R. Z.; Cheng, N. C.; Mu, S. C.; Sun, X. L. Tuning the dual-active sites of ZIF-67 derived porous nanomaterials for boosting oxygen catalysis and rechargeable Zn-air batteries. *Nano Res.* **2020**, *14*, 2353–2362.

[14] Xin, S. L.; Liu, Z. Q.; Ma, L.; Sun, Y.; Xiao, C. H.; Li, F.; Du, Y. P. Visualization of the electrocatalytic activity of three-dimensional $MoSe_2$@reduced graphene oxide hybrid nanostructures for oxygen reduction reaction. *Nano Res.* **2016**, *9*, 3795–3811.

[15] Meng, Z. H.; Chen, N.; Cai, S. C.; Wu, J. W.; Wang, R.; Tian, T.; Tang, H. L. Rational design of hierarchically porous Fe-N-doped carbon as efficient electrocatalyst for oxygen reduction reaction and Zn-air batteries. *Nano Res.* **2021**, *14*, 4768–4775.

[16] Xia, B. Y.; Yan, Y.; Li, N.; Wu, H. B.; Lou, X. W.; Wang, X. A metal-organic framework-derived bifunctional oxygen electrocatalyst. *Nat. Energy* **2016**, *1*, 15006.

[17] Gao, R. J.; Wang, J.; Huang, Z. F.; Zhang, R. R.; Wang, W.; Pan, L.; Zhang, J. F.; Zhu, W. K.; Zhang, X. W.; Shi, C. X. et al. Pt/Fe_2O_3 with Pt-Fe pair sites as a catalyst for oxygen reduction with ultralow Pt loading. *Nat. Energy* **2021**, *6*, 614–623.

[18] Jasinski, R. A new fuel cell cathode catalyst. *Nature* **1964**, *201*, 1212–1213.

[19] Gupta, S.; Tryk, D.; Bae, I.; Aldred, W.; Yeager, E. Heat-treated polyacrylonitrile-based catalysts for oxygen electroreduction. *J. Appl. Electrochem.* **1989**, *19*, 19–27.

[20] Luo, E. G.; Chu, Y. Y.; Liu, J.; Shi, Z. P.; Zhu, S. Y.; Gong, L. Y.; Ge, J. J.; Choi, C. H.; Liu, C. P.; Xing, W. Pyrolyzed M–N_x catalysts for oxygen reduction reaction: Progress and prospects. *Energy Environ. Sci.* **2021**, *14*, 2158–2185.

[21] Li, Z. Q.; Jiang, G. P.; Deng, Y. P.; Liu, G. H.; Ren, D. Z.; Zhang, Z.; Zhu, J. B.; Gao, R.; Jiang, Y.; Luo, D. et al. Deep-breathing honeycomb-like Co-N_x-C nanopolyhedron bifunctional oxygen electrocatalysts for rechargeable Zn-air batteries. *iScience* **2020**, *23*, 101404.

[22] Qin, J. Y.; Liu, H.; Zou, P. C.; Zhang, R.; Wang, C. Y.; Xin, H. L. Altering ligand fields in single-atom sites through second-shell anion modulation boosts the oxygen reduction reaction. *J. Am. Chem. Soc.* **2022**, *144*, 2197–2207.

[23] Cui, X.; Gao, L. K.; Lei, S.; Liang, S.; Zhang, J. W.; Sewell, C. D.; Xue, W. D.; Liu, Q.; Lin, Z. Q.; Yang, Y. K. Simultaneously crafting single-atomic Fe sites and graphitic layer-wrapped Fe_3C nanoparticles encapsulated within mesoporous carbon tubes for oxygen reduction. *Adv. Funct. Mater.* **2021**, *31*, 2009197.

[24] Xiao, M. L.; Zhu, J. B.; Li, G. R.; Li, N.; Li, S.; Cano, Z. P.; Ma, L.; Cui, P. X.; Xu, P.; Jiang, G. P. et al. A single-atom iridium heterogeneous catalyst in oxygen reduction reaction. *Angew. Chem., Int. Ed.* **2019**, *58*, 9640–9645.

[25] Liu, S. W.; Li, C. Z.; Zachman, M. J.; Zeng, Y. C.; Yu, H. R.; Li, B. Y.; Wang, M. Y.; Braaten, J.; Liu, J. W.; Meyer, H. M. et al. Atomically dispersed iron sites with a nitrogen-carbon coating as highly active and durable oxygen reduction catalysts for fuel cells. *Nat. Energy* **2022**, *7*, 652–663.

[26] Wu, G.; More, K. L.; Johnston, C. M.; Zelenay, P. High-performance electrocatalysts for oxygen reduction derived from polyaniline, iron, and cobalt. *Science* **2011**, *332*, 443–447.

[27] Zhang, Q. Q.; Guan, J. Q. Single-atom catalysts for electrocatalytic applications. *Adv. Funct. Mater.* **2020**, *30*, 2000768.

[28] Marshall-Roth, T.; Libretto, N. J.; Wrobel, A. T.; Anderton, K. J.; Pegis, M. L.; Ricke, N. D.; Voorhis, T. V.; Miller, J. T.; Surendranath, Y. A pyridinic Fe-N_4 macrocycle models the active sites in Fe/N-doped carbon electrocatalysts. *Nat. Commun.* **2020**, *11*, 5283.

[29] Liu, K.; Fu, J. W.; Lin, Y. Y.; Luo, T.; Ni, G. H.; Li, H. M.; Lin, Z.; Liu, M. Insights into the activity of single-atom Fe-N-C catalysts for oxygen reduction reaction. *Nat. Commun.* **2022**, *13*, 2075.

[30] Guo, D. H.; Shibuya, R.; Akiba, C.; Saji, S.; Kondo, T.; Nakamura,

J. Active sites of nitrogen-doped carbon materials for oxygen reduction reaction clarified using model catalysts. *Science* **2016**, *351*, 361–365.

[31] Chung, H. T.; Cullen, D. A.; Higgins, D.; Sneed, B. T.; Holby, E. F.; More, K. L.; Zelenay, P. Direct atomic-level insight into the active sites of a high-performance PGM-free ORR catalyst. *Science* **2017**, *357*, 479–484.

[32] Sun, Y. L.; Wang, J.; Liu, Q.; Xia, M. R.; Tang, Y. F.; Gao, F. M.; Hou, Y. L.; Tse, J.; Zhao, Y. F. Itinerant ferromagnetic half metallic cobalt-iron couples: Promising bifunctional electrocatalysts for ORR and OER. *J. Mater. Chem. A* **2019**, *7*, 27175–27185.

[33] Zhang, N.; Zhou, T. P.; Chen, M. L.; Feng, H.; Yuan, R. L.; Zhong, C. A.; Yan, W. S.; Tian, Y. C.; Wu, X. J.; Chu, W. S. et al. High-purity pyrrole-type FeN_4 sites as a superior oxygen reduction electrocatalyst. *Energy Environ. Sci.* **2020**, *13*, 111–118.

[34] Xie, X. H.; He, C.; Li, B. Y.; He, Y. H.; Cullen, D. A.; Wegener, E. C.; Kropf, A. J.; Martinez, U.; Cheng, Y. W.; Engelhard, M. H. et al. Performance enhancement and degradation mechanism identification of a single-atom Co-N-C catalyst for proton exchange membrane fuel cells. *Nat. Catal.* **2020**, *3*, 1044–1054.

[35] Tian, H.; Cui, X. Z.; Dong, H. L.; Meng, G.; Kong, F. T.; Chen, Y. F.; Peng, L. X.; Chen, C.; Chang, Z. W.; Shi, J. L. Engineering single MnN_4 atomic active sites on polydopamine-modified helical carbon tubes towards efficient oxygen reduction. *Energy Storage Mater.* **2021**, *37*, 274–282.

[36] Liu, S.; Li, Z. D.; Wang, C. L.; Tao, W. W.; Huang, M. X.; Zuo, M.; Yang, Y.; Yang, K.; Zhang, L. J.; Chen, S. et al. Turning main-group element magnesium into a highly active electrocatalyst for oxygen reduction reaction. *Nat. Commun.* **2020**, *11*, 938.

[37] Zhu, M. Z.; Zhao, C.; Liu, X. K.; Wang, X. L.; Zhou, F. Y.; Wang, J.; Hu, Y. M.; Zhao, Y. F.; Yao, T.; Yang, L. M. et al. Single atomic cerium sites with a high coordination number for efficient oxygen reduction in proton-exchange membrane fuel cells. *ACS Catal.* **2021**, *11*, 3923–3929.

[38] Lu, Z. Y.; Wang, B.; Hu, Y. F.; Liu, W.; Zhao, Y. F.; Yang, R. O.; Li, Z. P.; Luo, J.; Chi, B.; Jiang, Z. et al. An isolated zinc-cobalt atomic pair for highly active and durable oxygen reduction. *Angew. Chem., Int. Ed.* **2019**, *58*, 2622–2626.

[39] Chen, J. Y.; Li, H.; Fan, C.; Meng, Q. W.; Tang, Y. W.; Qiu, X. Y.; Fu, G. T.; Ma, T. Y. Dual single-atomic Ni-N_4 and Fe-N_4 sites constructing janus hollow graphene for selective oxygen electrocatalysis. *Adv. Mater.* **2020**, *32*, 2003134.

[40] Li, L. F.; Wen, Y. D.; Han, G. K.; Liu, Y. X.; Song, Y. J.; Zhang, W.; Sun, J.; Du, L.; Kong, F. P.; Ma, Y. L. et al. Tailoring the stability of Fe-N-C via pyridinic nitrogen for acid oxygen reduction reaction. *Chem. Eng. J.* **2022**, *437*, 135320.

[41] Wang, R. G.; Zhang, L. F.; Shan, J. Q.; Yang, Y. Y.; Lee, J. F.; Chen, T. Y.; Mao, J.; Zhao, Y.; Yang, L. J.; Hu, Z. P. et al. Tuning Fe spin moment in Fe-N-C catalysts to climb the activity volcano via a local geometric distortion strategy. *Adv. Sci.* **2022**, *9*, e2203917.

[42] Haile, A. S.; Hansen, H. A.; Yohannes, W.; Mekonnen, Y. S. The role of nitrogen and sulfur dual coordination of cobalt in Co-$N_{4-x}S_x$/C single atom catalysts in the oxygen reduction reaction. *Sustainable Energy Fuels* **2022**, *6*, 179–187.

[43] Li, L. B.; Huang, S. H.; Cao, R.; Yuan, K.; Lu, C. B.; Huang, B. Y.; Tang, X. N.; Hu, T.; Zhuang, X. D.; Chen, Y. W. Optimizing microenvironment of asymmetric N, S-coordinated single-atom Fe via axial fifth coordination toward efficient oxygen electroreduction. *Small* **2022**, *18*, 2105387.

[44] Wang, X.; Jia, Y.; Mao, X.; Liu, D. B.; He, W. X.; Li, J.; Liu, J. G.; Yan, X. C.; Chen, J.; Song, L. et al. Edge-rich Fe-N_4 active sites in defective carbon for oxygen reduction catalysis. *Adv. Mater.* **2020**, *32*, 2000966.

[45] Jiang, T.; Luan, W. L.; Turyanska, L.; Feng, Q. Enhanced electrocatalytic oxygen reduction reaction for Fe-N_4-C by the incorporation of Co nanoparticles. *Nanoscale* **2021**, *13*, 6521–6530.

[46] Xia, D. S.; Yang, X.; Xie, L.; Wei, Y. P.; Jiang, W. L.; Dou, M.; Li, X. N.; Li, J.; Gan, L.; Kang, F. Y. Direct growth of carbon nanotubes doped with single atomic Fe-N_4 active sites and neighboring graphitic nitrogen for efficient and stable oxygen reduction electrocatalysis. *Adv. Funct. Mater.* **2019**, *29*, 1906174.

[47] Yang, X.; Xia, D. S.; Kang, Y. Q.; Du, H. D.; Kang, F. Y.; Gan, L.; Li, J. Unveiling the axial hydroxyl ligand on Fe-N_4-C electrocatalysts and its impact on the pH-dependent oxygen reduction activities and poisoning kinetics. *Adv. Sci.* **2020**, *7*, 2000176.

[48] Xu, H. X.; Cheng, D. J.; Cao, D. P.; Zeng, X. C. A universal principle for a rational design of single-atom electrocatalysts. *Nat. Catal.* **2018**, *1*, 339–348.

[49] Zhao, C. X.; Li, B. Q.; Liu, J. N.; Zhang, Q. Intrinsic electrocatalytic activity regulation of M-N-C single-atom catalysts for the oxygen reduction reaction. *Angew. Chem., Int. Ed.* **2021**, *60*, 4448–4463.

[50] Lin, Y. Y.; Liu, K.; Chen, K. J.; Xu, Y.; Li, H. M.; Hu, J. H.; Lu, Y. R.; Chan, T. S.; Qiu, X. Q.; Fu, J. W. et al. Tuning charge distribution of FeN_4 via external N for enhanced oxygen reduction reaction. *ACS Catal.* **2021**, *11*, 6304–6315.

[51] Wang, X. X.; Wang, B.; Zhong, J.; Zhao, F. P.; Han, N.; Huang, W. J.; Zeng, M.; Fan, J.; Li, Y. G. Iron polyphthalocyanine sheathed multiwalled carbon nanotubes: A high-performance electrocatalyst for oxygen reduction reaction. *Nano Res.* **2016**, *9*, 1497–1506.

[52] Fu, X. G.; Li, N.; Ren, B. H.; Jiang, G. P.; Liu, Y. R.; Hassan, F. M.; Su, D.; Zhu, J. B.; Yang, L.; Bai, Z. Y. et al. Tailoring FeN_4 sites with edge enrichment for boosted oxygen reduction performance in proton exchange membrane fuel cell. *Adv. Energy Mater.* **2019**, *9*, 1803737.

[53] Jin, X. X.; Xie, Y.; Fu, J. H.; Zhao, C. Y.; Xu, Y. H.; Lv, Y.; Zhang, B. S.; Sun, K. J.; Si, R.; Huang, J. H. A highly efficient Fe-N-C electrocatalyst with atomically dispersed FeN_4 sites for the oxygen reduction reaction. *ChemCatChem* **2021**, *13*, 2683–2690.

[54] Qiao, M. F.; Wang, Y.; Wang, Q.; Hu, G. Z.; Mamat, X.; Zhang, S. S.; Wang, S. Y. Hierarchically ordered porous carbon with atomically dispersed FeN_4 for ultraefficient oxygen reduction reaction in proton-exchange membrane fuel cells. *Angew. Chem., Int. Ed.* **2020**, *59*, 2688–2694.

[55] Yin, H. B.; Yuan, P. F.; Lu, B. A.; Xia, H. C.; Guo, K.; Yang, G. G.; Qu, G.; Xue, D. P.; Hu, Y. F.; Cheng, J. Q. et al. Phosphorus-driven electron delocalization on edge-type FeN_4 active sites for oxygen reduction in acid medium. *ACS Catal.* **2021**, *11*, 12754–12762.

[56] Su, P. P.; Huang, W. J.; Zhang, J. W.; Guharoy, U.; Du, Q. G.; Sun, Q.; Jiang, Q. K.; Cheng, Y.; Yang, J.; Zhang, X. L. et al. Fe atoms anchored on defective nitrogen doped hollow carbon spheres as efficient electrocatalysts for oxygen reduction reaction. *Nano Res.* **2021**, *14*, 1069–1077.

[57] Adabi, H.; Shakouri, A.; Hassan, N. U.; Varcoe, J. R.; Zulevi, B.; Serov, A.; Regalbuto, J. R.; Mustain, W. E. High-performing commercial Fe-N-C cathode electrocatalyst for anion-exchange membrane fuel cells. *Nat. Energy* **2021**, *6*, 834–843.

[58] Wan, X.; Liu, X. F.; Li, Y. C.; Yu, R. H.; Zheng, L. R.; Yan, W. S.; Wang, H.; Xu, M.; Shui, J. L. Fe-N-C electrocatalyst with dense active sites and efficient mass transport for high-performance proton exchange membrane fuel cells. *Nat. Catal.* **2019**, *2*, 259–268.

[59] Snitkoff-Sol, R. Z.; Friedman, A.; Honig, H. C.; Yurko, Y.; Kozhushner, A.; Zachman, M. J.; Zelenay, P.; Bond, A. M.; Elbaz, L. Quantifying the electrochemical active site density of precious metal-free catalysts *in situ* in fuel cells. *Nat. Catal.* **2022**, *5*, 163–170.

[60] Jiao, L.; Li, J. K.; Richard, L. L.; Sun, Q.; Stracensky, T.; Liu, E. S.; Sougrati, M. T.; Zhao, Z. P.; Yang, F.; Zhong, S. C. et al. Chemical vapour deposition of Fe-N-C oxygen reduction catalysts with full utilization of dense Fe-N_4 sites. *Nat. Mater.* **2021**, *20*, 1385–1391.

[61] Ding, R.; Liu, Y. D.; Rui, Z. Y.; Li, J.; Liu, J. G.; Zou, Z. G. Facile grafting strategy synthesis of single-atom electrocatalyst with

enhanced ORR performance. *Nano Res.* **2020**, *13*, 1519–1526.
[62] Xiao, M. L.; Xing, Z. H.; Jin, Z.; Liu, C. P.; Ge, J. J.; Zhu, J. B.; Wang, Y.; Zhao, X.; Chen, Z. W. Preferentially engineering FeN_4 edge sites onto graphitic nanosheets for highly active and durable oxygen electrocatalysis in rechargeable Zn-air batteries. *Adv. Mater.* **2020**, *32*, e2004900.
[63] Xiao, M. L.; Zhu, J. B.; Ma, L.; Jin, Z.; Ge, J. J.; Deng, X.; Hou, Y.; He, Q. G.; Li, J. K.; Jia, Q. Y. et al. Microporous framework induced synthesis of single-atom dispersed Fe-N-C acidic ORR catalyst and its *in situ* reduced Fe-N_4 active site identification revealed by X-ray absorption spectroscopy. *ACS Catal.* **2018**, *8*, 2824–2832.
[64] Cai, H. Z.; Chen, B. B.; Zhang, X.; Deng, Y. C.; Xiao, D. Q.; Ma, D.; Shi, C. Highly active sites of low spin $Fe^{II}N_4$ species: The identification and the ORR performance. *Nano Res.* **2021**, *14*, 122–130.
[65] Li, J. K.; Sougrati, M. T.; Zitolo, A.; Ablett, J. M.; Oğuz, I. C.; Mineva, T.; Matanovic, I.; Atanassov, P.; Huang, Y.; Zenyuk, I. et al. Identification of durable and non-durable FeN_x sites in Fe-N-C materials for proton exchange membrane fuel cells. *Nat. Catal.* **2020**, *4*, 10–19.
[66] Zitolo, A.; Goellner, V.; Armel, V.; Sougrati, M. T.; Mineva, T.; Stievano, L.; Fonda, E.; Jaouen, F. Identification of catalytic sites for oxygen reduction in iron- and nitrogen-doped graphene materials. *Nat. Mater.* **2015**, *14*, 937–942.
[67] Xu, X. L.; Zhang, X. M.; Kuang, Z. C.; Xia, Z. X.; Rykov, A. I.; Yu, S. S.; Wang, J. H.; Wang, S. L.; Sun, G. Q. Investigation on the demetallation of Fe-N-C for oxygen reduction reaction: The influence of structure and structural evolution of active site. *Appl. Catal. B: Environ.* **2022**, *309*, 121290.
[68] Du, L.; Prabhakaran, V.; Xie, X. H.; Park, S.; Wang, Y.; Shao, Y. Y. Low-PGM and PGM-free catalysts for proton exchange membrane fuel cells: Stability challenges and material solutions. *Adv. Mater.* **2021**, *33*, e1908232.
[69] Xie, H.; Xie, X. H.; Hu, G. X.; Prabhakaran, V.; Saha, S.; Gonzalez-Lopez, L.; Phakatkar, A. H.; Hong, M.; Wu, M. L.; Shahbazian-Yassar, R. et al. Ta-TiO_x nanoparticles as radical scavengers to improve the durability of Fe-N-C oxygen reduction catalysts. *Nat. Energy* **2022**, *7*, 281–289.
[70] Li, X. H.; Yang, X. X.; Liu, L. T.; Zhao, H.; Li, Y. W.; Zhu, H. Y.; Chen, Y. Z.; Guo, S. W.; Liu, Y. N.; Tan, Q. et al. Chemical vapor deposition for N/S-doped single fe site catalysts for the oxygen reduction in direct methanol fuel cells. *ACS Catal.* **2021**, *11*, 7450–7459.
[71] Yu, L.; Li, Y. C.; Ruan, Y. F. Dynamic control of sacrificial bond transformation in the Fe-N-C single-atom catalyst for molecular oxygen reduction. *Angew. Chem., Int. Ed.* **2021**, *60*, 25296–25301.
[72] Yuan, K.; Lützenkirchen-Hecht, D.; Li, L. B.; Shuai, L.; Li, Y. Z.; Cao, R.; Qiu, M.; Zhuang, X. D.; Leung, M. K. H.; Chen, Y. W. et al. Boosting oxygen reduction of single iron active sites via geometric and electronic engineering: Nitrogen and phosphorus dual coordination. *J. Am. Chem. Soc.* **2020**, *142*, 2404–2412.
[73] Jin, Z. Y.; Li, P. P.; Meng, Y.; Fang, Z. W.; Xiao, D.; Yu, G. H. Understanding the inter-site distance effect in single-atom catalysts for oxygen electroreduction. *Nat. Catal.* **2021**, *4*, 615–622.
[74] Li, X. L.; Xiang, Z. H. Identifying the impact of the covalent-bonded carbon matrix to FeN_4 sites for acidic oxygen reduction. *Nat. Commun.* **2022**, *13*, 57.
[75] Chen, K. J.; Liu, K.; An, P. D.; Li, H. J. W.; Lin, Y. Y.; Hu, J. H.; Jia, C. K.; Fu, J. W.; Li, H. M.; Liu, H. et al. Iron phthalocyanine with coordination induced electronic localization to boost oxygen reduction reaction. *Nat. Commun.* **2020**, *11*, 4173.
[76] Wang, J.; Li, L. Q.; Chen, X.; Lu, Y. L.; Yang, W. S.; Duan, X. A Co-N/C hollow-sphere electrocatalyst derived from a metanilic CoAl layered double hydroxide for the oxygen reduction reaction, and its active sites in various pH media. *Nano Res.* **2017**, *10*, 2508–2518.
[77] He, Y. H.; Shi, Q. R.; Shan, W. T.; Li, X.; Kropf, A. J.; Wegener, E. C.; Wright, J.; Karakalos, S.; Su, D.; Cullen, D. A. et al. Dynamically unveiling metal–nitrogen coordination during thermal activation to design high-efficient atomically dispersed CoN_4 active sites. *Angew. Chem., Int. Ed.* **2021**, *60*, 9516–9526.
[78] Chen, L. Y.; Liu, X. F.; Zheng, L. R.; Li, Y. C.; Guo, X.; Wan, X.; Liu, Q. T.; Shang, J. X.; Shui, J. L. Insights into the role of active site density in the fuel cell performance of Co-N-C catalysts. *Appl. Catal. B: Environ.* **2019**, *256*, 117849.
[79] Xiao, G. F.; Lu, R. H.; Liu, J. F.; Liao, X. B.; Wang, Z. Y.; Zhao, Y. Coordination environments tune the activity of oxygen catalysis on single atom catalysts: A computational study. *Nano Res.* **2022**, *15*, 3073–3081.
[80] Mahsud, A.; Chen, J. N.; Yuan, X. L.; Lyu, F. L.; Zhong, Q. X.; Chen, J. X.; Yin, Y. D.; Zhang, Q. Self-templated formation of cobalt-embedded hollow N-doped carbon spheres for efficient oxygen reduction. *Nano Res.* **2021**, *14*, 2819–2825.
[81] Guo, L.; Hwang, S.; Li, B. Y.; Yang, F.; Wang, M. Y.; Chen, M. J.; Yang, X. X.; Karakalos, S. G.; Cullen, D. A.; Feng, Z. X. et al. Promoting atomically dispersed MnN_4 sites via sulfur doping for oxygen reduction: Unveiling intrinsic activity and degradation in fuel cells. *ACS Nano* **2021**, *15*, 6886–6899.
[82] Li, J. Z.; Chen, M. J.; Cullen, D. A.; Hwang, S.; Wang, M. Y.; Li, B. Y.; Liu, K. X.; Karakalos, S.; Lucero, M.; Zhang, H. G. et al. Atomically dispersed manganese catalysts for oxygen reduction in proton-exchange membrane fuel cells. *Nat. Catal.* **2018**, *1*, 935–945.
[83] Bai, L.; Duan, Z. Y.; Wen, X. D.; Si, R.; Guan, J. Q. Atomically dispersed manganese-based catalysts for efficient catalysis of oxygen reduction reaction. *Appl. Catal. B: Environ.* **2019**, *257*, 117930.
[84] Chen, M. J.; Li, X.; Yang, F.; Li, B. Y.; Stracensky, T.; Karakalos, S.; Mukerjee, S.; Jia, Q. Y.; Su, D.; Wang, G. F. et al. Atomically dispersed MnN_4 catalysts via environmentally benign aqueous synthesis for oxygen reduction: Mechanistic understanding of activity and stability improvements. *ACS Catal.* **2020**, *10*, 10523–10534.
[85] Vashistha, V. K.; Kumar, A. Design and synthesis of MnN_4 macrocyclic complex for efficient oxygen reduction reaction electrocatalysis. *Inorg. Chem. Commun.* **2020**, *112*, 107700.
[86] Yang, Y.; Mao, K. T.; Gao, S. Q.; Huang, H.; Xia, G. L.; Lin, Z. Y.; Jiang, P.; Wang, C. L; Wang, H.; Chen, Q. W. O-, N-atoms-coordinated Mn cofactors within a graphene framework as bioinspired oxygen reduction reaction electrocatalysts. *Adv. Mater.* **2018**, *30*, 1801732.
[87] Li, J.; Chen, S. G.; Yang, N.; Deng, M. M.; Ibraheem, S.; Deng, J. H.; Li, J.; Li, L.; Wei, Z. D. Ultrahigh-loading zinc single-atom catalyst for highly efficient oxygen reduction in both acidic and alkaline media. *Angew. Chem., Int. Ed.* **2019**, *58*, 7035–7039.
[88] Luo, E. G.; Zhang, H.; Wang, X.; Gao, L. Q.; Gong, L. Y.; Zhao, T.; Jin, Z.; Ge, J. J.; Jiang, Z.; Liu, C. P. et al. Single-atom Cr-N_4 sites designed for durable oxygen reduction catalysis in acid media. *Angew. Chem., Int. Ed.* **2019**, *58*, 12469–12475.
[89] Hu, J. W.; Cai, X. B.; Wu, J.; Xin, C. C.; Guo, J. Y.; Liu, Z. R.; Wei, J. Z.; Cheng, X. S.; Hao, C.; Dong, H. P. et al. Boosting oxygen-reduction catalysis over mononuclear CuN_{2+2} moiety for rechargeable Zn-air battery. *Chem. Eng. J.* **2022**, *430*, 133105.
[90] Lin, Z. Y.; Huang, H.; Cheng, L.; Hu, W.; Xu, P. P.; Yang, Y.; Li, J. M.; Gao, F. Y.; Yang, K.; Liu, S. et al. Tuning the p-orbital electron structure of s-block metal Ca enables a high-performance electrocatalyst for oxygen reduction. *Adv. Mater.* **2021**, *33*, 2107103.
[91] Luo, F.; Roy, A.; Silvioli, L.; Cullen, D. A.; Zitolo, A.; Sougrati, M. T.; Oguz, I. C.; Mineva, T.; Teschner, D.; Wagner, S. et al. P-block single-metal-site tin/nitrogen-doped carbon fuel cell cathode catalyst for oxygen reduction reaction. *Nat. Mater.* **2020**, *19*, 1215–1223.
[92] Gu, Y.; Xi, B. J.; Zhang, H.; Ma, Y. C.; Xiong, S. L. Activation of main-group antimony atomic sites for oxygen reduction catalysis. *Angew. Chem., Int. Ed.* **2022**, *61*, e202202200.
[93] Zhang, D.; Xie, X.; Sun, P. P.; Wei, Y. A.; Gong, T.; Huang, N.;

Lv, X. W.; Fang, L.; Sun, X. H. Atomically dispersed antimony on N-doped carbon for highly efficient oxygen reduction reaction. *Chem. Eng. J.* **2022**, *439*, 135700.

[94] Hu, H.; Wang, J. J.; Cui, B. F.; Zheng, X. R.; Lin, J. G.; Deng, Y. D.; Han, X. P. Atomically dispersed selenium sites on nitrogen-doped carbon for efficient electrocatalytic oxygen reduction. *Angew. Chem., Int. Ed.* **2022**, *61*, e202114441.

[95] Xiao, M. L.; Gao, L. Q.; Wang, Y.; Wang, X.; Zhu, J. B.; Jin, Z.; Liu, C. P.; Chen, H. Q.; Li, G. R.; Ge, J. J. et al. Engineering energy level of metal center: Ru single-atom site for efficient and durable oxygen reduction catalysis. *J. Am. Chem. Soc.* **2019**, *141*, 19800–19806.

[96] Wang, T. Z.; Cao, X. J.; Qin, H. Y.; Shang, L.; Zheng, S. Y.; Fang, F.; Jiao, L. F. P-block atomically dispersed antimony catalyst for highly efficient oxygen reduction reaction. *Angew. Chem., Int. Ed.* **2021**, *60*, 21237–21241.

[97] Deng, C. F.; Su, Y.; Li, F. H.; Shen, W. F.; Chen, Z. F.; Tang, Q. Understanding activity origin for the oxygen reduction reaction on bi-atom catalysts by DFT studies and machine-learning. *J. Mater. Chem. A* **2020**, *8*, 24563–24571.

[98] Xu, J.; Lai, S. H.; Qi, D. F.; Hu, M.; Peng, X. Y.; Liu, Y. F.; Liu, W.; Hu, G. Z.; Xu, H.; Li, F. et al. Atomic Fe-Zn dual-metal sites for high-efficiency pH-universal oxygen reduction catalysis. *Nano Res.* **2021**, *14*, 1374–1381.

[99] Xiao, M. L.; Zhang, H.; Chen, Y. T.; Zhu, J. B.; Gao, L. Q.; Jin, Z.; Ge, J. J.; Jiang, Z.; Chen, S. L.; Liu, C. P. et al. Identification of binuclear Co_2N_5 active sites for oxygen reduction reaction with more than one magnitude higher activity than single atom CoN_4 site. *Nano Energy* **2018**, *46*, 396–403.

[100] Xiao, M. L.; Zhu, J. B.; Li, S.; Li, G. R.; Liu, W. W.; Deng, Y. P.; Bai, Z. Y.; Ma, L.; Feng, M.; Wu, T. P. et al. 3d-Orbital occupancy regulated Ir-Co atomic pair toward superior bifunctional oxygen electrocatalysis. *ACS Catal.* **2021**, *11*, 8837–8846.

[101] Xiao, M. L.; Chen, Y. T.; Zhu, J. B.; Zhang, H.; Zhao, X.; Gao, L. Q.; Wang, X.; Zhao, J.; Ge, J. J.; Jiang, Z. et al. Climbing the apex of the ORR volcano plot via binuclear site construction: Electronic and geometric engineering. *J. Am. Chem. Soc.* **2019**, *141*, 17763–17770.

[102] Li, L.; Li, Y. M.; Huang, R.; Cao, X. R.; Wen, Y. H. Boosting the electrocatalytic activity of Fe-Co dual-atom catalysts for oxygen reduction reaction by ligand-modification engineering. *ChemCatChem* **2021**, *13*, 4645–4651.

[103] Zhou, Y. D.; Yang, W.; Utetiwabo, W.; Lian, Y. M.; Yin, X.; Zhou, L.; Yu, P. W.; Chen, R. J.; Sun, S. R. Revealing of active sites and catalytic mechanism in N-coordinated Fe, Ni dual-doped carbon with superior acidic oxygen reduction than single-atom catalyst. *J. Phys. Chem. Lett.* **2020**, *11*, 1404–1410.

[104] Yang, G. G.; Zhu, J. W.; Yuan, P. F.; Hu, Y. F.; Qu, G.; Lu, B. A.; Xue, X. Y.; Yin, H. B.; Cheng, W. Z.; Cheng, J. Q. et al. Regulating Fe-spin state by atomically dispersed Mn-N in Fe-N-C catalysts with high oxygen reduction activity. *Nat. Commun.* **2021**, *12*, 1734.

[105] Zhang, N.; Zhou, T. P.; Ge, J. K.; Lin, Y.; Du, Z. Y.; Zhong, C. A.; Wang, W. J.; Jiao, Q. Y.; Yuan, R. L.; Tian, Y. C. et al. High-density planar-like Fe_2N_6 structure catalyzes efficient oxygen reduction. *Matter* **2020**, *3*, 509–521.

[106] Cui, T. T.; Wang, Y. P.; Ye, T.; Wu, J.; Chen, Z. Q.; Li, J.; Lei, Y. P.; Wang, D. S.; Li, Y. D. Engineering dual single-atom sites on 2D ultrathin N-doped carbon nanosheets attaining ultra-low-temperature zinc-air battery. *Angew. Chem., Int. Ed.* **2022**, *61*, e202115219.

[107] Li, W. H.; Yang, J. R.; Wang, D. S. Long-range interactions in diatomic catalysts boosting electrocatalysis. *Angew. Chem., Int. Ed.* **2022**, *61*, e202213318.

[108] Han, A. L.; Wang, X. J.; Tang, K.; Zhang, Z. D.; Ye, C. L.; Kong, K. J.; Hu, H. B.; Zheng, L. R.; Jiang, P.; Zhao, C. X. et al. An adjacent atomic platinum site enables single-atom iron with high oxygen reduction reaction performance. *Angew. Chem., Int. Ed.* **2021**, *60*, 19262–19271.

[109] Fang, X. Z.; Jiao, L.; Yu, S. H.; Jiang, H. L. Metal-organic framework-derived feco-n-doped hollow porous carbon nanocubes for electrocatalysis in acidic and alkaline media. *ChemSusChem* **2017**, *10*, 3019–3024.

[110] Liu, M.; Li, N.; Cao, S. F.; Wang, X. M.; Lu, X. Q.; Kong, L. J.; Xu, Y. H.; Bu, X. H. A "pre-constrained metal twins" strategy to prepare efficient dual-metal-atom catalysts for cooperative oxygen electrocatalysis. *Adv. Mater.* **2022**, *34*, e2107421.

[111] Zhu, Z. J.; Yin, H. J.; Wang, Y.; Chuang, C. H.; Xing, L.; Dong, M. Y.; Lu, Y. R.; Casillas-Garcia, G.; Zheng, Y. L.; Chen, S. et al. Coexisting single-atomic fe and Ni sites on hierarchically ordered porous carbon as a highly efficient ORR electrocatalyst. *Adv. Mater.* **2020**, *32*, e2004670.

[112] Luo, F.; Zhu, J. B.; Ma, S. X.; Li, M.; Xu, R. Z.; Zhang, Q.; Yang, Z. H.; Qu, K. G.; Cai, W. W.; Chen, Z. W. Regulated coordination environment of Ni single atom catalyst toward high-efficiency oxygen electrocatalysis for rechargeable Zinc-air batteries. *Energy Storage Mater.* **2021**, *35*, 723–730.

[113] Cai, H. Z.; Zhang, G. H.; Zhang, X.; Chen, B. B.; Lu, Z.; Xu, H. J.; Gao, R.; Shi, C. Engineering the local coordination environment and density of FeN_4 sites by mn cooperation for electrocatalytic oxygen reduction. *Small* **2022**, *18*, e2200911.

[114] Tong, M. M.; Sun, F. F.; Xie, Y.; Wang, Y.; Yang, Y. Q.; Tian, C. G.; Wang, L.; Fu, H. G. Operando cooperated catalytic mechanism of atomically dispersed Cu-N_4 and Zn-N_4 for promoting oxygen reduction reaction.. *Angew. Chem., Int. Ed.* **2021**, *60*, 14005–14012.

[115] Sui, R.; Zhang, X. J.; Wang, X. D.; Wang, X. Y.; Pei, J. J.; Zhang, Y. F.; Liu, X. R.; Chen, W. X.; Zhu, W.; Zhuang, Z. B. Silver based single atom catalyst with heteroatom coordination environment as high performance oxygen reduction reaction catalyst. *Nano Res.* **2022**, *15*, 7968–7975.

[116] Wei, X.; Zheng, D.; Zhao, M.; Chen, H. Z.; Fan, X.; Gao, B.; Gu, L.; Guo, Y.; Qin, J. B.; Wei, J. et al. Cross-linked polyphosphazene hollow nanosphere-derived N/P-doped porous carbon with single nonprecious metal atoms for the oxygen reduction reaction. *Angew. Chem., Int. Ed.* **2020**, *59*, 14639–14646.

[117] Saputro, A. G.; Kasai, H.; Asazawa, K.; Kishi, H.; Tanaka, H. Comparative study on the catalytic activity of the TM-N_2 active sites (TM = Mn, Fe, Co, Ni) in the oxygen reduction reaction: Density functional theory study. *J. Phys. Soc. Japan* **2013**, *82*, 114704.

[118] Cai, Z. H.; Lin, S. X.; Xiao, J. J.; Muhmood, T.; Chen, Y. H.; Wang, Y. F.; Hu, X. B.; Zheng, L. R. Efficient bifunctional catalytic electrodes with uniformly distributed NiN_2 active sites and channels for long-lasting rechargeable zinc-air batteries. *Small* **2020**, *16*, e2002518.

[119] Zhang, M. T.; Li, H.; Chen, J. X.; Ma, F. X.; Zhen, L.; Wen, Z. H.; Xu, C. Y. Transition metal (Co, Ni, Fe, Cu) single-atom catalysts anchored on 3D nitrogen-doped porous carbon nanosheets as efficient oxygen reduction electrocatalysts for Zn-air battery. *Small* **2022**, *18*, e2202476.

[120] Sun, X. X.; Li, K.; Yin, C.; Wang, Y.; He, F.; Tang, H.; Wu, Z. J. CoN_3 embedded graphene, a potential catalyst for the oxygen reduction reaction from a theoretical perspective. *Phys. Chem. Chem. Phys.* **2017**, *19*, 17670–17676.

[121] Lai, S. J.; Xu, L.; Liu, H. L.; Chen, S.; Cai, R. S.; Zhang, L. J.; Theis, W.; Sun, J.; Yang, D. J.; Zhao, X. L. Controllable synthesis of CoN_3 catalysts derived from Co/Zn-ZIF-67 for electrocatalytic oxygen reduction in acidic electrolytes. *J. Mater. Chem. A* **2019**, *7*, 21884–21891.

[122] Mohammadi-Rad, N.; Esrafili, M. D.; Sardroodi, J. J. CuN_3 doped graphene as an active electrocatalyst for oxygen reduction reaction in fuel cells: A DFT study. *J. Mol. Graph. Model.* **2020**, *96*, 107537.

[123] Li, Y. C.; Liu, X. F.; Zheng, L. R.; Shang, J. X.; Wan, X.; Hu, R. M.; Guo, X.; Hong, S.; Shui, J. L. Preparation of Fe-N-C catalysts with FeN_x (x = 1, 3, 4) active sites and comparison of their activities for the oxygen reduction reaction and performances in proton exchange membrane fuel cells. *J. Mater. Chem. A* **2019**, *7*,

26147–26153.
[124] Han, Y. L.; Li, Q. K.; Ye, K.; Luo, Y.; Jiang, J.; Zhang, G. Z. Impact of active site density on oxygen reduction reactions using monodispersed Fe-N-C single-atom catalysts. *ACS Appl. Mater. Interfaces* **2020**, *12*, 15271–15278.
[125] Liang, X.; Li, Z. Y.; Xiao, H.; Zhang, T. F.; Xu, P.; Zhang, H.; Gao, Q. M.; Zheng, L. R. Two types of single-atom FeN_4 and FeN_5 electrocatalytic active centers on n-doped carbon driving high performance of the SA-Fe-NC oxygen reduction reaction catalyst. *Chem. Mater.* **2021**, *33*, 5542–5554.
[126] Zhang, H. N.; Jia, S. P.; Shi, X. L.; Li, Z. Y.; Liu, B.; Li, N.; Li, Y.; Hu, S. L.; Wang, H. Q. Atomic Fe-N_5 catalytic sites embedded in N-doped carbon as a highly efficient oxygen electrocatalyst for zinc-air batteries. *Mater. Chem. Front.* **2021**, *5*, 8127–8137.
[127] Huang, J. S.; Lu, Q. Q.; Ma, X.; Yang, X. R. Bio-inspired FeN_5 moieties anchored on a three-dimensional graphene aerogel to improve oxygen reduction catalytic performance. *J. Mater. Chem. A* **2018**, *6*, 18488–18497.
[128] Li, L.; Chen, Y. J.; Xing, H. R.; Li, N.; Xia, J. W.; Qian, X. Y.; Xu, H.; Li, W. Z.; Yin, F. X.; He, G. Y. et al. Single-atom Fe-N_5 catalyst for high-performance zinc-air batteries. *Nano Res.* **2022**, *15*, 8056–8064.
[129] Zhu, Y. S.; Zhang, B. S.; Liu, X.; Wang, D. W.; Su, D. S. Unravelling the structure of electrocatalytically active Fe-N complexes in carbon for the oxygen reduction reaction. *Angew. Chem., Int. Ed.* **2014**, *53*, 10673–10677.
[130] Yang, L.; Cheng, D. J.; Xu, H. X.; Zeng, X. F.; Wan, X.; Shui, J. L.; Xiang, Z. H.; Cao, D. P. Unveiling the high-activity origin of single-atom iron catalysts for oxygen reduction reaction. *Proc. Natl. Acad. Sci. USA* **2018**, *115*, 6626–6631.
[131] Liu, K. X.; Wu, G.; Wang, G. F. Role of local carbon structure surrounding FeN_4 sites in boosting the catalytic activity for oxygen reduction. *J. Phys. Chem. C* **2017**, *121*, 11319–11324.
[132] Ha, Y.; Fei, B.; Yan, X. X.; Xu, H. B.; Chen, Z. L.; Shi, L. X.; Fu, M. S.; Xu, W.; Wu, R. B. Atomically dispersed Co-pyridinic N-C for superior oxygen reduction reaction. *Adv. Energy Mater.* **2020**, *10*, 2002592.
[133] Zhang, J.; Yang, J. Y.; Wang, Y.; Lu, H. Q.; Zhang, M. G. Catalytic mechanism of oxygen reduction on two types of CoN_4-graphene: A density functional study. *Int. J. Energy Res.* **2021**, *45*, 10858–10868.
[134] Chen, Y. J.; Gao, R.; Ji, S. F.; Li, H. J.; Tang, K.; Jiang, P.; Hu, H. B.; Zhang, Z. D.; Hao, H. G.; Qu, Q. Y. et al. Atomic-level modulation of electronic density at cobalt single-atom sites derived from metal-organic frameworks: Enhanced oxygen reduction performance. *Angew. Chem., Int. Ed.* **2021**, *60*, 3212–3221.
[135] Hu, B. T.; Huang, A. J.; Zhang, X. J.; Chen, Z.; Tu, R. Y.; Zhu, W.; Zhuang, Z. B.; Chen, C.; Peng, Q.; Li, Y. D. Atomic Co/Ni dual sites with N/P-coordination as bifunctional oxygen electrocatalyst for rechargeable zinc-air batteries. *Nano Res.* **2021**, *14*, 3482–3488.
[136] Wang, J.; Li, H. G.; Liu, S. H.; Hu, Y. F.; Zhang, J.; Xia, M. R.; Hou, Y. L.; Tse, J.; Zhang, J. J.; Zhao, Y. F. Turning on Zn 4s electrons in a N_2-Zn-B_2 configuration to stimulate remarkable ORR performance. *Angew. Chem., Int. Ed.* **2021**, *60*, 181–185.
[137] Zhang, H.; Sun, Q. D.; He, Q.; Zhang, Y.; He, X. H.; Gan, T.; Ji, H. B. Single Cu atom dispersed on S, N-codoped nanocarbon derived from shrimp shells for highly-efficient oxygen reduction reaction. *Nano Res.* **2022**, *15*, 5995–6000.
[138] Zhi, Q. J.; Jiang, R.; Liu, W. P.; Sun, T. T.; Wang, K.; Jiang, J. Z. Atomic CoN_3S_1 sites for boosting oxygen reduction reaction via an atomic exchange strategy. *Nano Res.* **2022**, *15*, 1803–1808.
[139] Zhuang, Z. C.; Xia, L. X.; Huang, J. Z.; Zhu, P.; Li, Y.; Ye, C. L.; Xia, M. G.; Yu, R. H.; Lang, Z. Q.; Zhu, J. X. et al. Continuous modulation of electrocatalytic oxygen reduction activities of single-atom catalysts through p–n junction rectification. *Angew. Chem., Int. Ed.* **2023**, *135*, e202212335.
[140] Zhou, X. Y.; Xu, C.; Guo, P. P.; Sun, W. L.; Wei, P. J.; Liu, J. G. Axial ligand coordination tuning of the electrocatalytic activity of iron porphyrin electrografted onto carbon nanotubes for the oxygen reduction reaction. *Chem. —Eur. J.* **2021**, *27*, 9898–9904.
[141] Zhang, W. L.; Meeus, E. J.; Wang, L.; Zhang, L. H.; Yang, S. C.; de Bruin, B.; Reek, J. N. H.; Yu, F. S. Boosting electrochemical oxygen reduction performance of iron phthalocyanine through axial coordination sphere interaction. *ChemSusChem* **2022**, *15*, e202102379.
[142] Zhao, K. M.; Liu, S. Q.; Li, Y. Y.; Wei, X. L.; Ye, G. Y.; Zhu, W. W.; Su, Y. K.; Wang, J.; Liu, H. T.; He, Z. et al. Insight into the mechanism of axial ligands regulating the catalytic activity of Fe-N_4 sites for oxygen reduction reaction. *Adv. Energy Mater.* **2022**, *12*, 2103588.
[143] Liu, Y. R.; Liu, X. J.; Lv, Z. H.; Liu, R.; Li, L. H.; Wang, J. M.; Yang, W. X.; Jiang, X.; Feng, X.; Wang, B. Tuning the spin state of the iron center by bridge-bonded Fe-O-Ti ligands for enhanced oxygen reduction. *Angew. Chem., Int. Ed.* **2022**, *134*, e202117617.
[144] Chen, C.; Yang, X. D.; Zhou, Z. Y.; Lai, Y. J.; Rauf, M.; Wang, Y.; Pan, J.; Zhuang, L.; Wang, Q.; Wang, Y. C. et al. Aminothiazole-derived N, S, Fe-doped graphene nanosheets as high performance electrocatalysts for oxygen reduction. *Chem. Commun.* **2015**, *51*, 17092–17095.
[145] Chen, P. Z.; Zhou, T. P.; Xing, L. L.; Xu, K.; Tong, Y.; Xie, H.; Zhang, L. D.; Yan, W. S.; Chu, W. S.; Wu, C. Z. et al. Atomically dispersed iron-nitrogen species as electrocatalysts for bifunctional oxygen evolution and reduction reactions. *Angew. Chem., Int. Ed.* **2017**, *56*, 610–614.
[146] Kwak, D. H.; Han, S. B.; Lee, Y. W.; Park, H. S.; Choi, I. A.; Ma, K. B.; Kim, M. C.; Kim, S. J.; Kim, D. H.; Sohn, J. I. et al. Fe/N/S-doped mesoporous carbon nanostructures as electrocatalysts for oxygen reduction reaction in acid medium. *Appl. Catal. B: Environ.* **2017**, *203*, 889–898.
[147] Li, Y. H.; Chen, B. X.; Duan, X. Z.; Chen, S. M.; Liu, D. B.; Zang, K. T.; Si, R.; Lou, F. L.; Wang, X. H.; Rønning, M. et al. Atomically dispersed Fe-N-P-C complex electrocatalysts for superior oxygen reduction. *Appl. Catal. B: Environ.* **2019**, *249*, 306–315.
[148] Liu, S. Y.; Yang, H. T.; Yao, L.; Peng, H. L.; Huang, P. R.; Lin, X. C.; Liu, L. H.; Zhang, H. Z.; Cai, P.; Wen, X. et al. Design of Fe and Cu bimetallic integration on N and F co-doped porous carbon material for oxygen reduction reaction. *Int. J. Hydrogen Energy* **2022**, *47*, 7751–7760.
[149] Fu, S. F.; Zhu, C. Z.; Song, J. H.; Engelhard, M. H.; Li, X. L.; Zhang, P. N.; Xia, H. B.; Du, D.; Lin, Y. H. Template-directed synthesis of nitrogen- and sulfur-codoped carbon nanowire aerogels with enhanced electrocatalytic performance for oxygen reduction. *Nano Res.* **2017**, *10*, 1888–1895.
[150] Yang, L. P.; Zhang, X.; Yu, L. X.; Hou, J. H.; Zhou, Z.; Lv, R. T. Atomic Fe-N_4/C in flexible carbon fiber membrane as binder-free air cathode for Zn-air batteries with stable cycling over 1000 h. *Adv. Mater.* **2022**, *34*, e2105410.
[151] Chen, Z. Y.; Niu, H.; Ding, J.; Liu, H.; Chen, P. H.; Lu, Y. H.; Lu, Y. R.; Zuo, W. B.; Han, L.; Guo, Y. Z. et al. Unraveling the origin of sulfur-doped Fe-N-C single-atom catalyst for enhanced oxygen reduction activity: Effect of iron spin-state tuning. *Angew. Chem., Int. Ed.* **2021**, *60*, 25404–25410.
[152] Mun, Y.; Lee, S.; Kim, K.; Kim, S.; Lee, S.; Han, J. W.; Lee, J. Versatile strategy for tuning ORR activity of a single Fe-N_4 site by controlling electron-withdrawing/donating properties of a carbon plane. *J. Am. Chem. Soc.* **2019**, *141*, 6254–6262.
[153] Shen, H. J.; Gracia-Espino, E.; Ma, J. Y.; Zang, K. T.; Luo, J.; Wang, L.; Gao, S. S.; Mamat, X.; Hu, G. Z.; Wagberg, T. et al. Synergistic effects between atomically dispersed Fe-N-C and C-S-C for the oxygen reduction reaction in acidic media. *Angew. Chem., Int. Ed.* **2017**, *56*, 13800–13804.
[154] Jin, H. H.; Zhou, H.; Li, W. Q.; Wang, Z. H.; Yang, J. L.; Xiong, Y. L.; He, D. P.; Chen, L.; Mu, S. C. *In situ* derived Fe/N/S-codoped carbon nanotubes from ZIF-8 crystals as efficient electrocatalysts for the oxygen reduction reaction and zinc-air batteries.. *J. Mater. Chem. A* **2018**, *6*, 20093–20099.
[155] Wang, J.; Wang, Q. J.; She, W. X.; Xie, C. Y.; Zhang, X. Y.; Sun, M. C.; Xiao, J. W.; Wang, S. Tuning the electron density

distribution of the Co-N-C catalysts through guest molecules and heteroatom doping to boost oxygen reduction activity. *J. Power Sources* **2019**, *418*, 50–60.

[156] Jin, H. H.; Zhou, H.; Ji, P. X.; Zhang, C. T.; Luo, J. H.; Zeng, W. H.; Hu, C. X.; He, D. P.; Mu, S. C. ZIF-8/$LiFePO_4$ derived Fe-N-P Co-doped carbon nanotube encapsulated Fe_2P nanoparticles for efficient oxygen reduction and Zn-air batteries.. *Nano Res* **2020**, *13*, 818–823.

[157] Li, J. C.; Zhong, H.; Xu, M. J.; Li, T.; Wang, L. G.; Shi, Q. R.; Feng, S.; Lyu, Z. Y.; Liu, D.; Du, D. et al. Boosting the activity of Fe-N_x moieties in Fe-N-C electrocatalysts via phosphorus doping for oxygen reduction reaction. *Sci. China Mater.* **2020**, *63*, 965–971.

[158] Sun, H.; Liu, S. S.; Wang, M. F.; Qian, T.; Xiong, J.; Yan, C. L. Updating the intrinsic activity of a single-atom site with a P–O bond for a rechargeable Zn-air battery. *ACS Appl. Mater. Interfaces* **2019**, *11*, 33054–33061.

[159] Diao, Y. X.; Liu, H. M.; Yao, Z. X.; Liu, Y. S.; Hu, G. X.; Zhang, Q. F.; Li, Z. Tri-(Fe/F/N)-doped porous carbons as electrocatalysts for the oxygen reduction reaction in both alkaline and acidic media. *Nanoscale* **2020**, *12*, 18826–18833.

[160] Lee, Y. G.; Ahn, H. J. Tri(Fe/N/F)-doped mesoporous carbons as efficient electrocatalysts for the oxygen reduction reaction. *Appl. Surf. Sci.* **2019**, *487*, 389–397.

[161] Tao, X. F.; Lu, R. H.; Ni, L. M.; Gridin, V.; Al-Hilfi, S. H.; Qiu, Z. J.; Zhao, Y.; Kramm, U. I.; Zhou, Y. Z.; Mullen, K. Facilitating the acidic oxygen reduction of Fe-N-C catalysts by fluorine-doping. *Mater. Horiz.* **2022**, *9*, 417–424.

[162] Zhao, Y. M.; Liao, L. M.; Yu, G. Q.; Wei, P. J.; Liu, J. G. B-doped Fe/N/C porous catalyst for high-performance oxygen reduction in anion-exchange membrane fuel cells. *ChemElectroChem* **2019**, *6*, 1754–1760.

[163] Zhao, X.; Li, X.; Bi, Z. H.; Wang, Y. W.; Zhang, H. B.; Zhou, X. H.; Wang, Q.; Zhou, Y. T.; Wang, H. S.; Hu, G. Z. Boron modulating electronic structure of FeN_4C to initiate high-efficiency oxygen reduction reaction and high-performance zinc-air battery. *J. Energy Chem.* **2022**, *66*, 514–524.

[164] Sun, H.; Wang, M. F.; Du, X. C.; Jiao, Y.; Liu, S. S.; Qian, T.; Yan, Y. C.; Liu, C.; Liao, M.; Zhang, Q. H. et al. Modulating the d-band center of boron doped single-atom sites to boost the oxygen reduction reaction. *J. Mater. Chem. A* **2019**, *7*, 20952–20957.

[165] Zhang, W.; Mao, K. K.; Zeng, X. C. B-doped MnN_4-G nanosheets as bifunctional electrocatalysts for both oxygen reduction and oxygen evolution reactions.. *ACS Sustainable Chem. Eng.* **2019**, *7*, 18711–18717.

[166] Yuan, K.; Sfaelou, S.; Qiu, M.; Lützenkirchen-Hecht, D.; Zhuang, X. D.; Chen, Y. W.; Yuan, C.; Feng, X. L.; Scherf, U. Synergetic contribution of Boron and Fe-N_x species in porous carbons toward efficient electrocatalysts for oxygen reduction reaction. *ACS Energy Lett.* **2018**, *3*, 252–260.

[167] Chen, Z. Y.; Su, X. Z.; Ding, J.; Yang, N.; Zuo, W. B.; He, Q. Y.; Wei, Z. M.; Zhang, Q.; Huang, J.; Zhai, Y. M. Boosting oxygen reduction reaction with Fe and Se dual-atom sites supported by nitrogen-doped porous carbon. *Appl. Catal. B: Environ.* **2022**, *308*, 121206.

[168] Ni, W. P.; Gao, Y.; Zhang, Y.; Younus, H. A.; Guo, X. G.; Ma, C.; Zhang, Y.; Duan, J. F.; Zhang, J. H.; Zhang, S. G. O-doping boosts the electrochemical oxygen reduction activity of a single fe site in hydrophilic carbon with deep mesopores.. *ACS Appl. Mater. Interfaces* **2019**, *11*, 45825–45831.

[169] Chen, Y. J.; Ji, S. F.; Zhao, S.; Chen, W. X.; Dong, J. C.; Cheong, W. C.; Shen, R. A.; Wen, X. D.; Zheng, L. R.; Rykov, A. I. et al. Enhanced oxygen reduction with single-atomic-site iron catalysts for a zinc-air battery and hydrogen-air fuel cell. *Nat. Commun.* **2018**, *9*, 5422.

[170] Han, Y. H.; Wang, Y. G.; Xu, R. R.; Chen, W. X.; Zheng, L. R.; Han, A. J.; Zhu, Y. Q.; Zhang, J.; Zhang, H. B.; Luo, J. et al. Electronic structure engineering to boost oxygen reduction activity by controlling the coordination of the central metal. *Energy Environ. Sci.* **2018**, *11*, 2348–2352.

[171] Zhang, E. H.; Tao, L.; An, J. K.; Zhang, J. W.; Meng, L. Z.; Zheng, X. B.; Wang, Y.; Li, N.; Du, S. X.; Zhang, J. T. et al. Engineering the local atomic environments of indium single-atom catalysts for efficient electrochemical production of hydrogen peroxide. *Angew. Chem., Int. Ed.* **2022**, *61*, e202117347.

[172] Zong, L. B.; Fan, K. C.; Wu, W. C.; Cui, L. X.; Zhang, L. L.; Johannessen, B.; Qi, D. C.; Yin, H. J.; Wang, Y.; Liu, P. R. et al. Anchoring single copper atoms to microporous carbon spheres as high-performance electrocatalyst for oxygen reduction reaction. *Adv. Funct. Mater.* **2021**, *31*, 2104864.

[173] Jiang, R.; Li, L.; Sheng, T.; Hu, G. F.; Chen, Y. G.; Wang, L. Y. Edge-site engineering of atomically dispersed Fe-N_4 by selective C–N bond cleavage for enhanced oxygen reduction reaction activities. *J. Am. Chem. Soc.* **2018**, *140*, 11594–11598.

[174] Yuan, S.; Zhang, J. W.; Hu, L. Y.; Li, J. N.; Li, S. W.; Gao, Y. N.; Zhang, Q. H.; Gu, L.; Yang, W. X.; Feng, X. et al. Decarboxylation-induced defects in MOF-derived single cobalt atom@carbon electrocatalysts for efficient oxygen reduction. *Angew. Chem., Int. Ed.* **2021**, *60*, 21685–21690.

[175] Ma, L. G.; Li, J. L.; Zhang, Z. W.; Yang, H.; Mu, X. Q.; Gu, X. Y.; Jin, H. H.; Chen, D.; Yan, S. L.; Liu, S. L. et al. Atomically dispersed dual Fe centers on nitrogen-doped bamboo-like carbon nanotubes for efficient oxygen reduction. *Nano Res.* **2022**, *15*, 1966–1972.

[176] Liu, X.; Liu, H.; Chen, C.; Zou, L. L.; Li, Y.; Zhang, Q.; Yang, B.; Zou, Z. Q.; Yang, H. Fe_2N nanoparticles boosting FeN_x moieties for highly efficient oxygen reduction reaction in Fe-N-C porous catalyst. *Nano Res.* **2019**, *12*, 1651–1657.

[177] Wan, X.; Liu, Q. T.; Liu, J. Y.; Liu, S. Y.; Liu, X. F.; Zheng, L. R.; Shang, J. X.; Yu, R. H.; Shui, J. L. Iron atom-cluster interactions increase activity and improve durability in Fe-N-C fuel cells. *Nat. Commun.* **2022**, *13*, 2963.

[178] Zheng, H. Z.; Ma, F.; Yang, H. C.; Wu, X. G.; Wang, R.; Jia, D. L.; Wang, Z. X.; Lu, N. D.; Ran, F.; Peng, S. L. Mn, N co-doped Co nanoparticles/porous carbon as air cathode for highly efficient rechargeable Zn-air batteries. *Nano Res.* **2022**, *15*, 1942–1948.

[179] Pan, Y.; Li, M.; Mi, W. L.; Wang, M. M.; Li, J. X.; Zhao, Y. L.; Ma, X. L.; Wang, B.; Zhu, W.; Cui, Z. M. et al. Single-atomic Mn sites coupled with Fe_3C nanoparticles encapsulated in carbon matrixes derived from bimetallic Mn/Fe polyphthalocyanine conjugated polymer networks for accelerating electrocatalytic oxygen reduction. *Nano Res.* **2022**, *15*, 7976–7985.

[180] Cheng, Q. Q.; Han, S. B.; Mao, K.; Chen, C.; Yang, L. J.; Zou, Z. Q.; Gu, M.; Hu, Z.; Yang, H. Co nanoparticle embedded in atomically-dispersed Co-N-C nanofibers for oxygen reduction with high activity and remarkable durability. *Nano Energy* **2018**, *52*, 485–493.

[181] Wang, Z.; Zhu, C.; Tan, H.; Liu, J.; Xu, L. L.; Zhang, Y. Q.; Liu, Y. P.; Zou, X. X.; Liu, Z.; Lu, X. H. Understanding the synergistic effects of cobalt single atoms and small nanoparticles: Enhancing oxygen reduction reaction catalytic activity and stability for zinc-air batteries. *Adv. Funct. Mater.* **2021**, *31*, 2104735.

[182] Ao, X.; Zhang, W.; Li, Z. S.; Li, J. G.; Soule, L.; Huang, X.; Chiang, W. H.; Chen, H. M.; Wang, C. D.; Liu, M. L. et al. Markedly enhanced oxygen reduction activity of single-atom Fe catalysts via integration with Fe nanoclusters. *ACS Nano* **2019**, *13*, 11853–11862.

[183] Huang, H. J.; Yu, D. S.; Hu, F.; Huang, S. C.; Song, J. N.; Chen, H. Y.; Li, L. L.; Peng, S. J. Clusters induced electron redistribution to tune oxygen reduction activity of transition metal single-atom for metal-air batteries. *Angew. Chem., Int. Ed.* **2022**, *61*, e202116068.

[184] Sun, X. P.; Wei, P.; Gu, S. Q.; Zhang, J. X.; Jiang, Z.; Wan, J.; Chen, Z. Y.; Huang, L.; Xu, Y.; Fang, C. et al. Atomic-level Fe-N-C coupled with Fe_3C-Fe nanocomposites in carbon matrixes as high-efficiency bifunctional oxygen catalysts. *Small* **2020**, *16*, e1906057.

[185] Cheng, X. Y.; Yang, J.; Yan, W.; Han, Y.; Qu, X. M.; Yin, S. H.; Chen, C.; Ji, R. Y.; Li, Y. R.; Li, G. et al. Nano-geometric deformation and synergistic Co nanoparticles Co-N_4 composite sites for proton exchange membrane fuel cells. *Energy Environ. Sci.* **2021**, *14*, 5958–5967.